Programmable intracellular DNA biocomputing circuits for reliable cell recognitions

Xue Gong,[a] *Jie Wei,*[a] *Jing Liu*[b]*, Ruomeng Li,*[a] *Xiaoqing Liu,*[a] *Fuan Wang**,[a]

[a] Key Laboratory of Analytical Chemistry for Biology and Medicine (Ministry of Education),

College of Chemistry and Molecular Sciences, Wuhan University, Wuhan, P. R. China

[b] Department of Gastroenterology, Zhongnan Hospital of Wuhan University, Hubei Clinical

Center & Key Lab of Intestinal & Colorectal Diseases, Wuhan, P. R. China

[*] To whom correspondence should be addressed. E-mail: fuanwang@whu.edu.cn.

Table of Contents

Supplementary Experimental Section

Native Polyacrylamide Gel Electrophoresis (PAGE): After the samples were prepared, 10 μL of each sample was mixed with 2 μL of 6×loading buffer, and then 10μL of the mixed solution was loaded into the notches of the freshly prepared 9% native polyacrylamide gel for electrophoresis analysis. Electrophoresis was performed at a constant voltage of 120V for 3.5 h in 1×TBE buffer (89 mM Tris, 89 mM BoricAcid, 2.0 mM EDTA, pH 8.3), followed by staining with GelRed for 20 min. Photographic images were obtained using FluorChem FC3 (ProteinSimple, USA) under 365 nm UV irradiation.

Atomic force microscopy (AFM) imaging: To distinguish the morphology of the assembled products, these different samples were respectively prepared in reaction buffer (10 mM HEPES, 1 M NaCl, 50 mM MgCl$_2$, pH 7.2) that contained miR-21 input (20 nM) and **H$_A$+H$_1$+H$_2$+H$_3$+H$_4$+H$_5$+H$_6$** (100 nM each) and characterized by AFM. The DNA sample was diluted and deposited on the freshly cleaved mice that was already treated with MgCl$_2$ (5 mM) for 2 min to bear positive charges on its surface for sample loading, and the samples allowed to absorb on the mica surface for 15 min. Then, the mice was rinsing with ddH$_2$O for three times and drying under a stream of nitrogen. AFM imaging was performed in air at room temperature with a tapping mode on Multimode 8 Atomic Force Microscope with a NanoScope V controller (Bruker Inc.). The silicon tips used for AFM analysis were SCANASYST-AIR (tip radius: ~2 nm; resonance frequency: ~70 kHz; spring constant: ~0.4 N/m; length: 115 μm; width: 25 μm).

Confocal laser scanning microscopy (CLSM) characterization: The Fluorescence Resonance Energy Transfer (FRET) imaging was performed using Leica TCS-SP8 laser scanning confocal microscopy system (Leica, Germany). All cellular images were obtained under 63.0×1.40 objective with oil. A 488 nm laser accompanying emission ranging from 500 to 550 nm was used as the excitation source of the green channel of fluorophore (FAM) donor. Acceptor (TAMRA) fluorescence image was obtained in red channel with 561 nm excitation accompanying emission ranging from 570 to 640 nm. The external 488 nm FRET stimulation with an accompanying emission signal collection ranging from 570 to 640 nm was selected for the yellow channel of TAMRA acceptor. The mean fluorescence intensity of cells is determined by averaging the fluorescence intensity of a large amount of randomly selected cells.

Quantitative Reverse transcription-PCR (qRT-PCR) analysis of miRNA in cells: The total RNAs were extracted in A549, MCF-7, MDA-MB-231 and MRC-5 using Trizol Reagent Kit (Invitrogen) according to the manufacturer's instructions. The cDNA were prepared by using Mir-X miRNA First-Strand Synthesis Kit (TaKaRa) according to the indicated protocol. The 5' primers used were: miR-21(TAGCT TATCA GACTG ATGTT GA); miR-155 (TTAAT GCTAA TCGTG ATAGG GGT) and the 3' primers of the two miRNAs for qPCR is the mRQ3' Primer supplied with the kit. PCR amplification was performed on the CFX96^{TM} Real-Time System (Bio-Rad) with following conditions: an initial 95 °C for 3 min followed by 40 cycles of 95 °C for 6 s, 60 °C for 20 s and 72 °C for 15 s. Relative expression levels of miR-21 and miR-155 were normalized using the U6 small RNA as the endogenous control.

Table S1 Sequences of the oligonucleotides for *in vitro* miRNAs-triggered DNA circuits.

Name	Sequence (5'-3')
miR-155	UUAAU GCUAA UCGUG AUAGG GGU
miR-21	UAGCU UAUCA GACUG AUGUU GA
H₁	GGAAT TCGGA GCTAG GTAGG TAGAG TAATG CCGTC TACCT ACCTA GCTCC G
H₂	GCTTC ATCTT CATCT CCGTC TACCT ACCTA GCTCC GAATT CCCGG AGCTA GGTAG GTAGA CGGCA TTACA CACTC
H₃	GAGTG TCGGA GATGA AGATG AAGCC ATCGT GCTTC ATCTT CATCT CCG-**TAMRA**
H₄	GCTTC ATCTT CATCT CCGGT TTTGC GGAGA TGAAG ATGAA GCACG ATG
H₅	**FAM**-CAAAA CCGGA GATGA AGATG AAGCT TGCCT GCTTC ATCTT CATCT CCG
H₆	GCTTC ATCTT CATCT CCGAC ACTCC GGAGA TGAAG ATGAA GCAGG CAA
H₇	TCGGA GCATT CAGTA CCGTC TACCT ACCTA GCTCC GAATT CCCGG AGCTA GGTAG GTAGA CGGCA TTACA CACTC
H_A	*TCTAC CTACC TAGCT CCGAA TTCC*T CAACA TCAGT CTGAT AAGCT ATTCG GAGCT AG
H_A'	*TCTAC CTACC TAGCT CCGAA TTCC*A CCCCT ATCAC GATTA GCATT AATTC GGAGC TAG
H_B	AGCCA CCAGT GCCCC AACCC CTATC ACGAT TAGCA TTAAT GGGGC ACTGG TG*GCT CCGAA TTCC*
H_C	AGCCA CCAGT GCCCC ATCAA CATCA GTCTG ATAAG CTATG GGGCA CTGGT G*GCTC CGAAT TCC*
L	*TCTAC CTACC TA*CAC CAGTG CCCCA
H_D	*TCTAC CTACC TA*CAC CAGTG CCCCA ACCCC TATCA CGATT AGCAT TAA TGGGGC ACTGG TGTAG
H_E	CTGGA GGCAG TCACC CCTAT CACGA TTAGC ATTAA GACTG CCTCC AGTCT ACCTA CCTAC ACCAG TGCCC CA
H_F	*CGGCA TTAC*C TGGAG GCAGT CTCAA CATCA GTCTG ATAAG CTAGA CTGCC TCCAG
I₃	GCTTC ATCTT CATCT TACTG A ATGC TCCGA
I₄	GAGTG TCGGA GATGA AGATG AAGC
I₅	CATCG TGCTT CATCT TCATC TCCG
Let-7a	UGAGG UAGUA GGUUG UAUAG UU
SM-3	UAGCU UAUCA *CUG*UG AUGUU GA
SM-2	UAG*A*U UAUCA GA*U*UG AUGUU GA
SM-1	UAGCU UAUCA *C*ACUG AUGUU GA

The underlined nucleotides represent the complementary parts
The bold italic nucleotides of SM indicates the mismatched sequence

Table S2 Sequences of the oligonucleotides for intracellular biocomputing circuits.

Name	Sequence (5'-3')
H₁	G*G*A* ATT CGG AGC TAG GTA GGT AGA GTA ATG CCG TCT ACC TAC CTA GCT *C*C*G
H₂	G*C*T* TCA TCT TCA TCT CCG TCT ACC TAC CTA GCT CCG AAT TCC CGG AGC TAG GTA GGT AGA CGG CAT TAC ACA *C*T*C
H₃	G*A*G* TGT CGG AGA TGA AGA TGA AGC CAT CGT GCT TCA TCT TCA TCT *C*C*G-**TAMRA**
H₄	G*C*T* TCA TCT TCA TCT CCG GTT TTG CGG AGA TGA AGA TGA AGC ACG *A*T*G
H₅	**FAM**-C*A*A* AAC CGG AGA TGA AGA TGA AGC TTG CCT GCT TCA TCT TCA TCT *C*C*G
H₆	G*C*T* TCA TCT TCA TCT CCG ACA CTC CGG AGA TGA AGA TGA AGC AGG *C*A*A
H₇	T*C*G*GA GCATT CAGTA CCGTC TACCT ACCTA GCTCC GAATT CCCGG AGCTA GGTAG GTAGA CGGCA TTACA CAC*T*C*
H_A	*T*C*T*AC CTACC TAGCT CCGAA TTCC*T CAACA TCAGT CTGAT AAGCT A*TTCG GAGCT* A*G*
H_B	A*G*C*CA CCAGT GCCCC A*ACCC CTATC ACGAT TAGCA TTAA*T GGGGC ACTGG TG*GCT CCGAA TT*C*C*
H_C	A*G*C*CA CCAGT GCCCC A*TCAA CATCA GTCTG ATAAG CTA*TG GGGCA CTGGT G*GCTC CGAAT T*C*C*
L	*T*C*T*ACCTACCTA*CACCA GTGCC C*C*A*
H_D	*T*C*T*AC CTACC TA*CAC CAGTG CCCCA ACCCC TATCA CGATT AGCAT TAA TGGGGC ACTGG TG*T*A*G*
H_E	C*T*G*GA GGCAG TC*ACC CCTAT CACGA TTAGC ATTAA GACTG CCTCC AG*TCT ACCTA CCTA*C ACCAG TGCCC* C*A*
H_F	*C*G*G*CA TTAC*C TGGAG GCAGT C*TCAA CATCA GTCTG ATAAG CTA*GA CTGCC TCC*A*G*
I₃	G*C*T*TC ATCTT CATCT TACTG A ATGC TCC*G*A*
I₄	G*A*G*TG TCGGA GATGA AGATG AA*G*C*
I₅	C*A*T*CG TGCTT CATCT TCATC TC*C*G*
miR-155 inhibitor	mA*mC*mC*mCmCmCmUmAmUmCmAmCmGmAmUmUmAmGmCmAm UmU*mA*mA*
miR-21 inhibitor	mU*mC*mA*mAmCmAmUmCmAmGmUmCmUmGmAmUmAmA mG*mC*mU *mA

* = Phosphorothioate Bonds
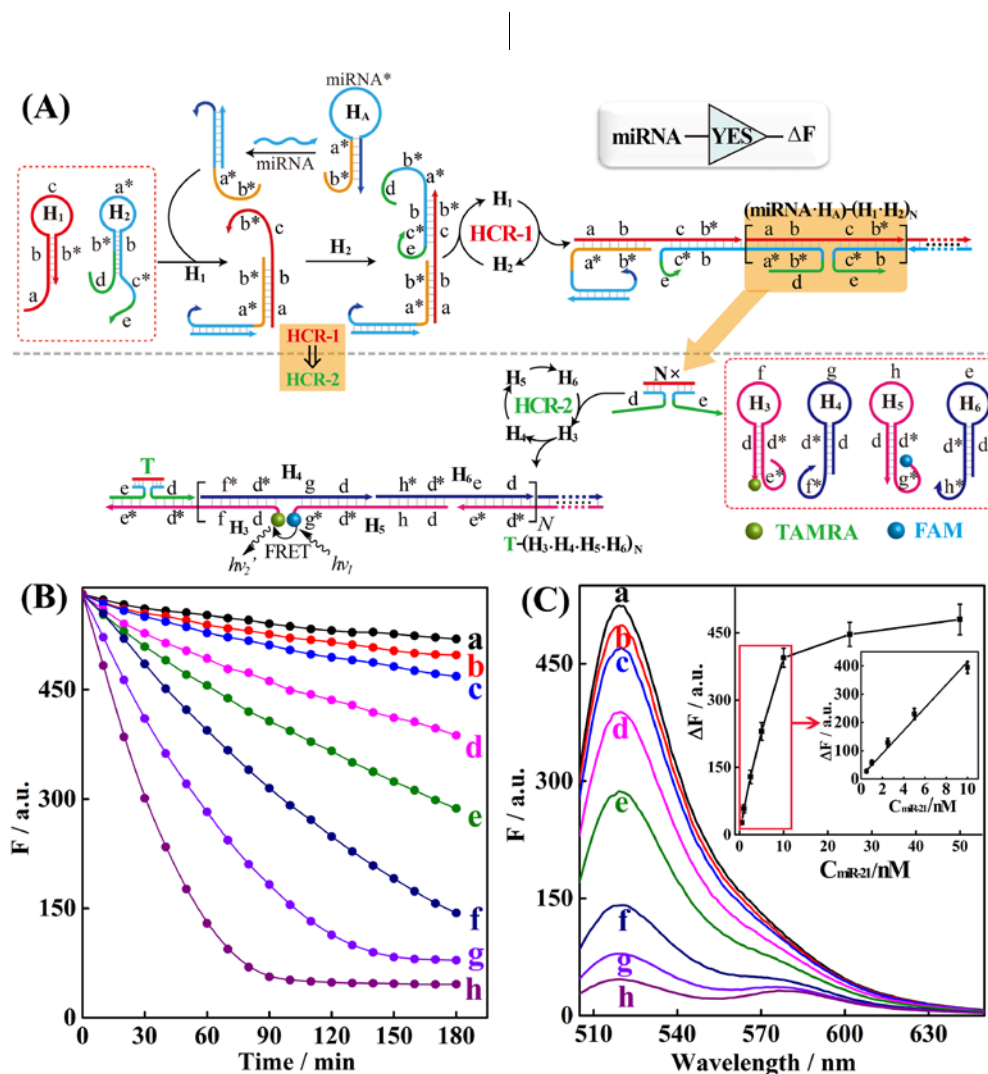
mN = 2'-*O*-Me RNA base

Figure S1. (**A**) Schematic illustration of the working principle for miR-21-assembled YES gate**. (B)** Time-dependent fluorescence changes (at λ=520 nm) of our proposed YES gate devices upon analyzing different concentrations of miR-21 target: (a) 0 nM (b) 0.5 nM, (c) 1 nM, (d) 2.5 nM, (e) 5 nM, (f) 10 nM, (g) 25 nM, (h) 50 nM. (**C**) The corresponding fluorescence spectra of (B) at a fixed time interval of 180 min. Inset: resulting calibration curve. Error bars were derived from n = 3 experiments.

The fluorescence of the miR-21-mediated YES gate system was examined upon their incubation with different concentrations of miR-21. According to Figure S1, elevated concentration of the target miRNA result in more substantial decreased FAM fluorescence intensity. The detection limit were estimated to be 150 pM for miR-21 according to the 3σ calculation method. These results confirm that the present strategy can obtained for sensitive miRNA detection.
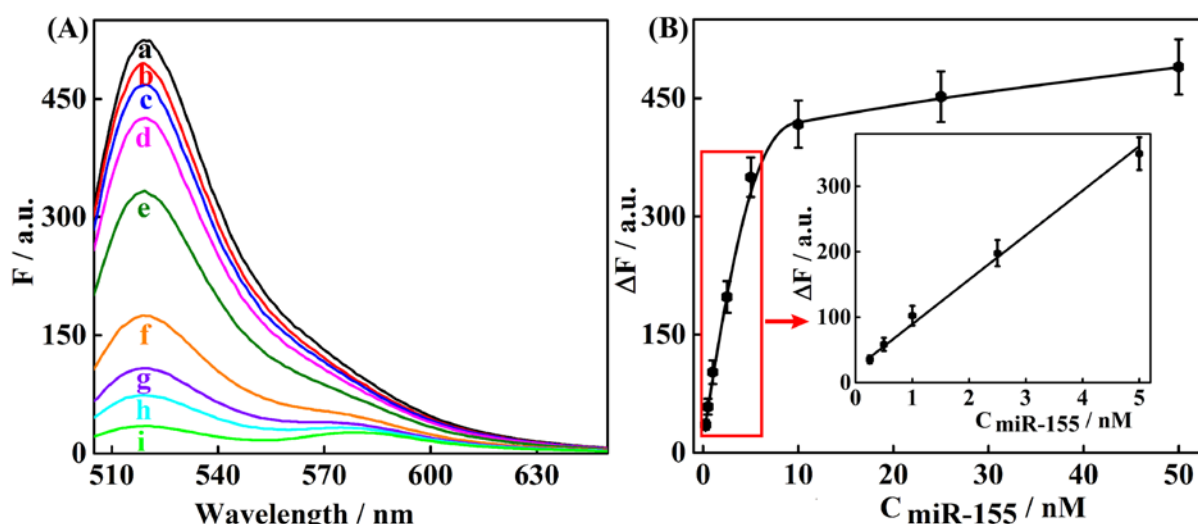
Figure S2. **(A)** Fluorescence spectra generated by the proposed miR-155-initiated YES gate devices upon analyzing different concentrations of miR-155 target: (a) 0 nM (b) 0.25 nM, (c) 0.5 nM, (d) 1 nM, (e) 2.5 nM, (f) 5 nM, (g) 10 nM, (h) 25 nM, (i) 50 nM. **(B)** Resulting calibration curve. Error bars were derived from n = 3 experiments.

It should be noted that the modular feature of our cascaded HCR enables us to detect any targeting biomarkers through redesigning the sensing module. For example, the miR-21-mediated YES gate could be facilely adapted to detect another important endogenous miRNA (miR-155) by redesigning the miR-21-recognition hairpin to miR-155-recognition hairpin without changing the amplified processing module. As shown in Figure S2, miR-155 could be sensitively detected in the dynamic range from 0.25 nM to 50 nM with a detection limit corresponding to 76 pM, demonstrating the cascaded HCR system can be used as a general amplification platform for sensitively detection of various analyst.
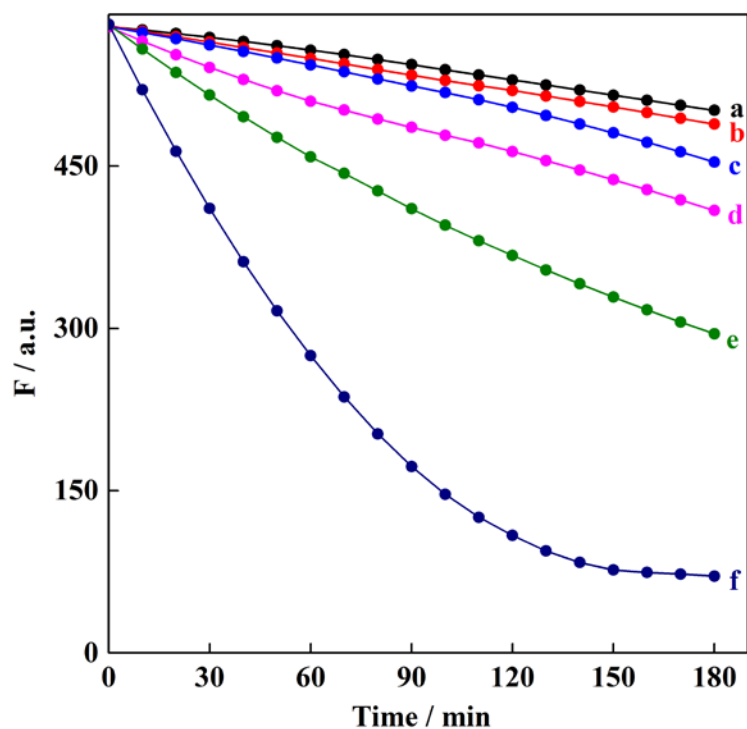
Figure S3. Time-dependent fluorescence changes (at λ=520 nm) of the miR-21-initiated YES gate system upon analyzing of different analytes: (a) no input, (b) 25 nM let-7a, (c) 25 nM SM-3, (d) 25 nM SM-2, (e) 25 nM SM-1, (f) 25 nM miR-21.

The selectivity of our amplification miR-21-initiated YES gate system was evaluated by using four control miRNA sequences, including let-7a, one, two and three-base mismatched miR-21 sequences. Figure S3 shows the time-dependent fluorescence changes upon introducing 25 nM miR-21 and its control counterparts. The results shown here clearly demonstrate the high selectivity of the designed system toward the target miRNA.
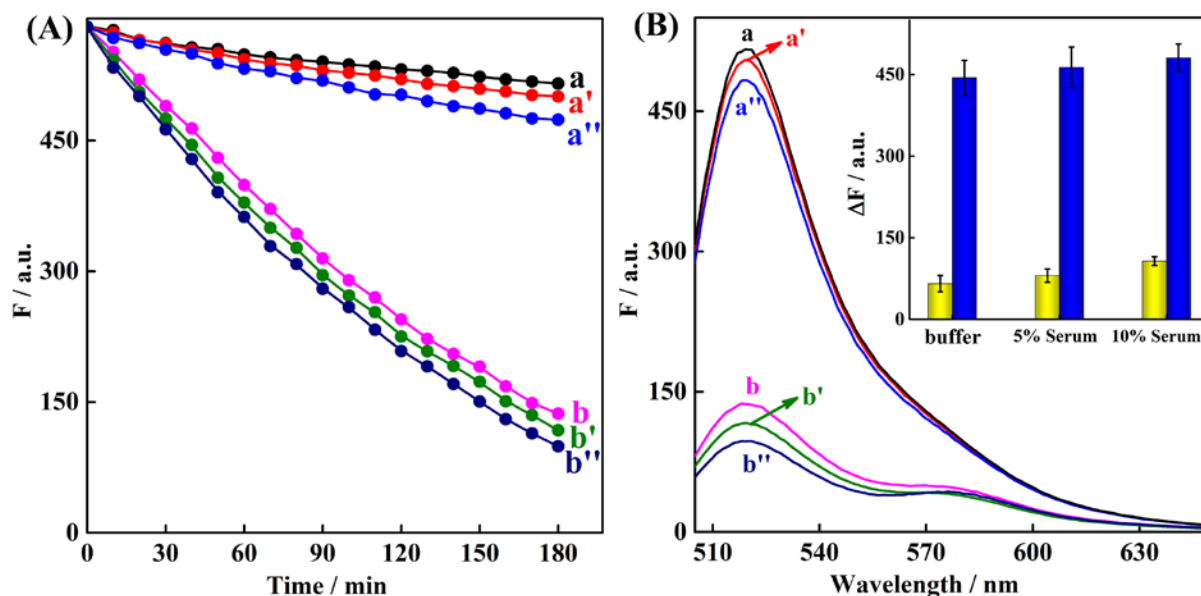
Figure S4. **(A)** Time-dependent fluorescence changes (at λ=520 nm) of the YES gate system upon analyzing miR-21 in different serum solutions: (a) buffer without miR-21, (b) 10 nM miR-21 in buffer, (a′) 5% serum without miR-21, (b′) 10 nM miR-21 in 5% serum, (a″) 10% serum without miR-21, and (b″) 10 nM miR -21 in 10% serum. **(B)** Summery of the fluorescence intensity changes (at λ=520 nm) as shown in Figure S3 (A) after a fixed time interval of 3h.

To verify whether the proposed strategy can be applied to monitor miRNA in complex biologic conditions, human serum samples were diluted with buffer and analyzed in 5% or 10% serum solutions, respectively. As displayed in Figure S4, even in 10% serum samples have a neglect interference compared to the blank test, indicating an acceptable accuracy of the designed HCR system for quantify biomarkers in complex biological fluids and may provide great practical application in clinic diagnosis of disease.
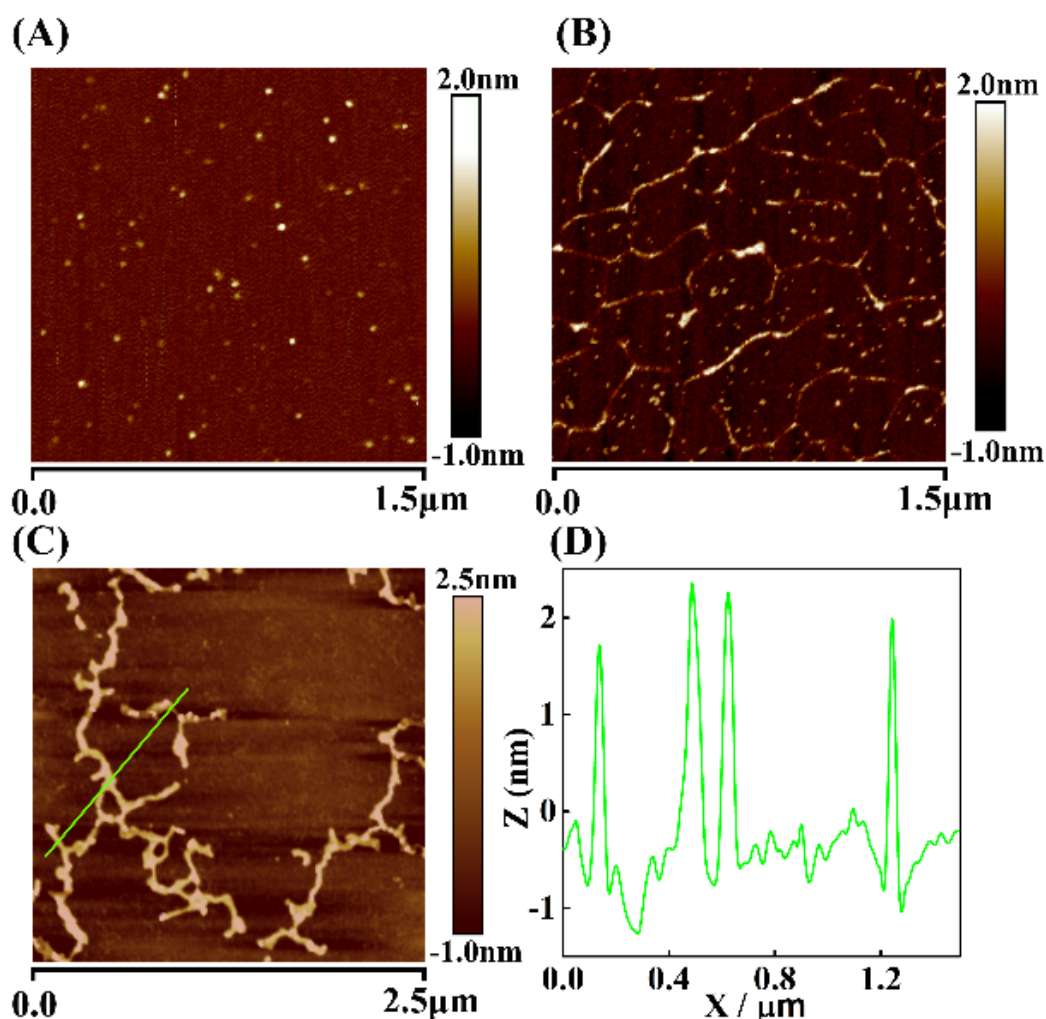
Figure S5. **(A)** AFM image of the HCR mixture without miR-21 target. **(B)** AFM characterization of upstream HCR-1-motivated linear dsDNA nanowires. **(C)** AFM image of the cascaded HCR product and **(D)** corresponding cross-section analysis.

The morphology of the miR-21-assembled DNA products was also characterized by AFM, Figure S5. In the absence of the miRNA-input, we can only see some tiny spots randomly distributed on the mica surface suggesting the stable coexistence of the hairpin subunits (Figure S5A). Importantly, when miR-21 is introduced into the single-layered HCR system, linear dsDNA structures were obtained (Figure S5B). On the contrary, different sizes of comb-like branched dsDNA nanowires with a height of around 2 nm were obtained upon introducing input miR-21 into the processing system (Figure S5C). The morphology of the assembled products demonstrated that input-motivated cascaded HCR enables branched growth of chain-like dsDNA nanostructures. Noted that the morphologies and size of the assembled dendrimers were polydisperse attribute to the random assembly of the hairpin subunits which, therefore, also obtained a few smaller linear dsDNA nanowire.
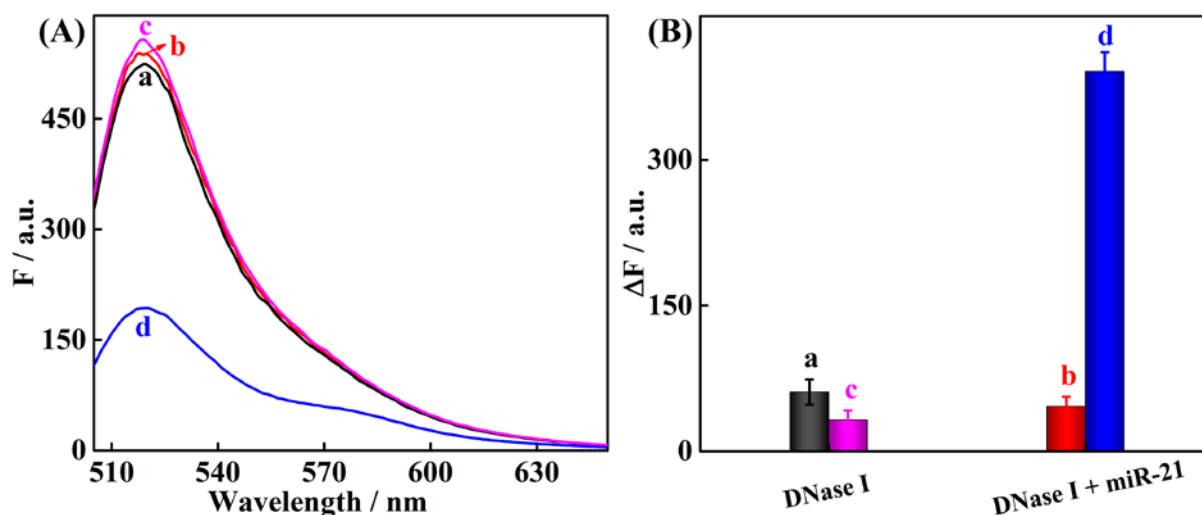
Figure S6. (**A**) Fluorescence spectra of the miR-21-initiated YES operation by (a) non-phosphorothioate DNA probes treated with DNase I (20 U) and (c) an additional miR-21 (10 nM), (b) phosphorothioate DNA probes treated with DNase I (20 U) and (d) an additional miR-21 (10 nM). (**B**) Summery of the fluorescence changes (at λ=520 nm) as shown in **Figure S6 (A)**.

To ensure the sufficient biostability of these biocomputing constructs (e.g., hairpin probes) in cell culture medium, all DNA probes were synthesized with phosphorothioate bonds for the subsequent intracellular imaging experiments. The effect of this phosphorothioate modification on DNase I-mediated digestion was explored and shown in **Figure S6**. After these non-phosphorothioate DNA probes were treated by DNase I (20 U), the corresponding miR-21 (10 nM) analyte triggers a slightly change of the fluorescence intensity, indicating that the DNase I mediates the degradation of the unmodified probe. On the contrary, the addition of miR-21 to the 20 U DNase I-treated phosphorothioate DNA probe causes a significant fluorescence change, demonstrating the phosphorothioate DNA probes are encoded with greatly improved tolerance in delaying nuclease degradation. These results suggest that these phosphorothioate DNA probe could ensure the potential intracellular detection of varied miRNAs expression patterns.
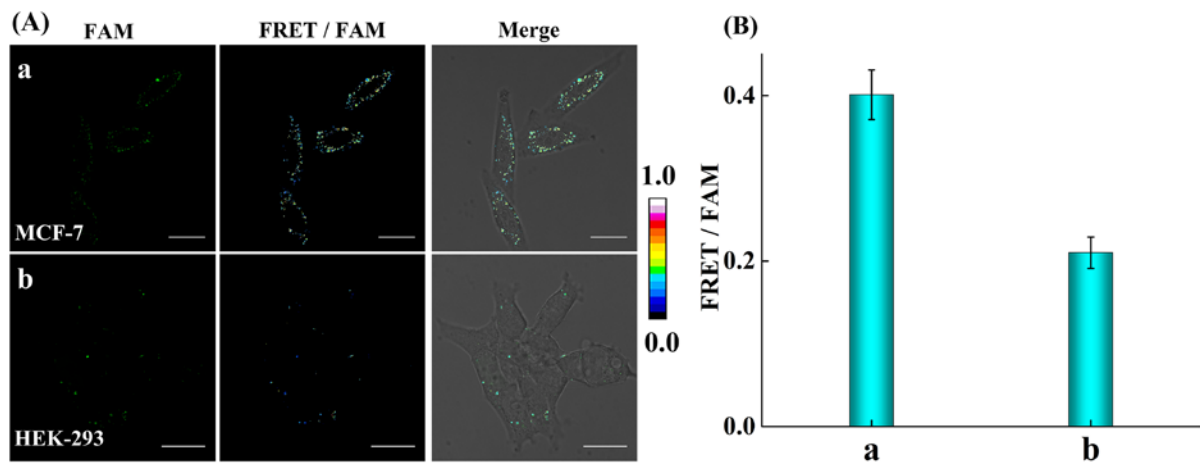
Figure S7. (A) Living cell analysis of the miRNA-initiated FRET transduction in (a) MCF-7 and (b) HEK-293 cells. **(B)** Statistical histogram analysis of the relative fluorescence intensity (FRET/FAM) of the MCF-7 and HEK-293 cells.
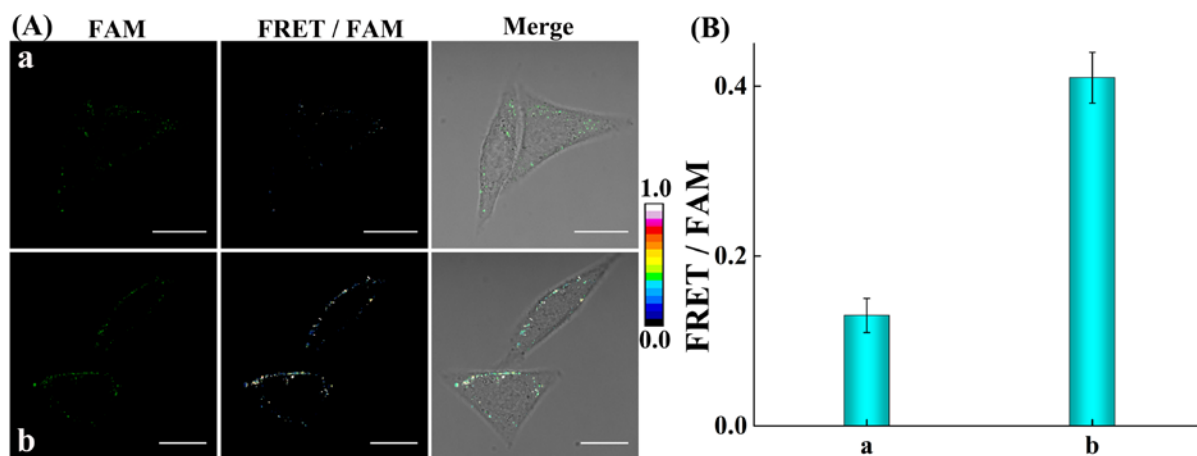
Figure S8. (**A**) Living cell analysis of miR-21 in MCF-7 cells that were respectively transfected with the **H₆**-excluded YES gate system (a) and the intact YES gate system (b). (**B**) Statistical histogram analysis of the relative fluorescence intensity (FRET/FAM) of the above two different cell samples.

To check the high amplified efficiency of the miR-21-initiated YES gate system, control experiment was carried out. A slightly weak FRET signal was obtained for conventional HCR imaging system (sample a in Figure S8) while an apparent FRET signal was obtained in MCF-7 cells upon incubation the cascaded HCR system (sample b in Figure S8), demonstrating the amplification efficacy of the cascaded HCR imaging platform is indeed enhanced over that of the conventional linear HCR imaging system.

Figure S9. FRET analysis of MCF-7 cells by z-stacks: (a) the green donor channel were collected from 500 to 550 nm with an 488 nm excitation, related to FAM dye; (b) the red acceptor channel were collected from 570 to 640 nm with an 561 excitation, related to TAMRA dye; (c) the yellow FRET channel were obtained from 570 to 640 nm with an 488 nm excitation; (d) FRET readout in the form of the fluorescence ratio of FRET to FAM (FRET/FAM). Scale bar = 20 μm.

MiRNAs-initiated OR gate operating

L	+	−	−	−	−	−	−	−	−	−	+	+	+	+
H$_C$	−	+	−	−	−	−	−	−	−	−	+	+	+	+
H$_B$	−	−	+	−	−	−	−	−	−	−	+	+	+	+
H$_1$	−	−	−	+	−	−	−	−	−	+	+	+	+	+
H$_2$	−	−	−	−	+	−	−	−	−	+	+	+	+	+
H$_3$	−	−	−	−	−	+	−	−	−	+	+	+	+	+
H$_4$	−	−	−	−	−	−	+	−	−	+	+	+	+	+
H$_5$	−	−	−	−	−	−	−	+	−	+	+	+	+	+
H$_6$	−	−	−	−	−	−	−	−	+	+	+	+	+	+
I$_1$	−	−	−	−	−	−	−	−	−	−	−	+	−	+
I$_2$	−	−	−	−	−	−	−	−	−	−	−	−	+	+

Figure S10. Native gel electrophoresis characterization of the OR logic gate. The "+" and "-" denote the presence and absence of the corresponding nucleic acid components, respectively.

The designed OR gate was confirmed by native polyacrylamide gel electrophoresis (PAGE) as shown in Figure S10. We can observe that almost no new band emerged for hairpin mixtures in the absence of inputs, indicating the stable coexistence of hairpins. However, when either just one or both inputs (miR-155 or miR-21) are presented, the bands of monomer hairpins became weakened and even vanished while a clear band close to the notch with lower electrophoretic mobility is obtained, demonstrating the reliability of our miRNA-initiated biocomputing circuits.
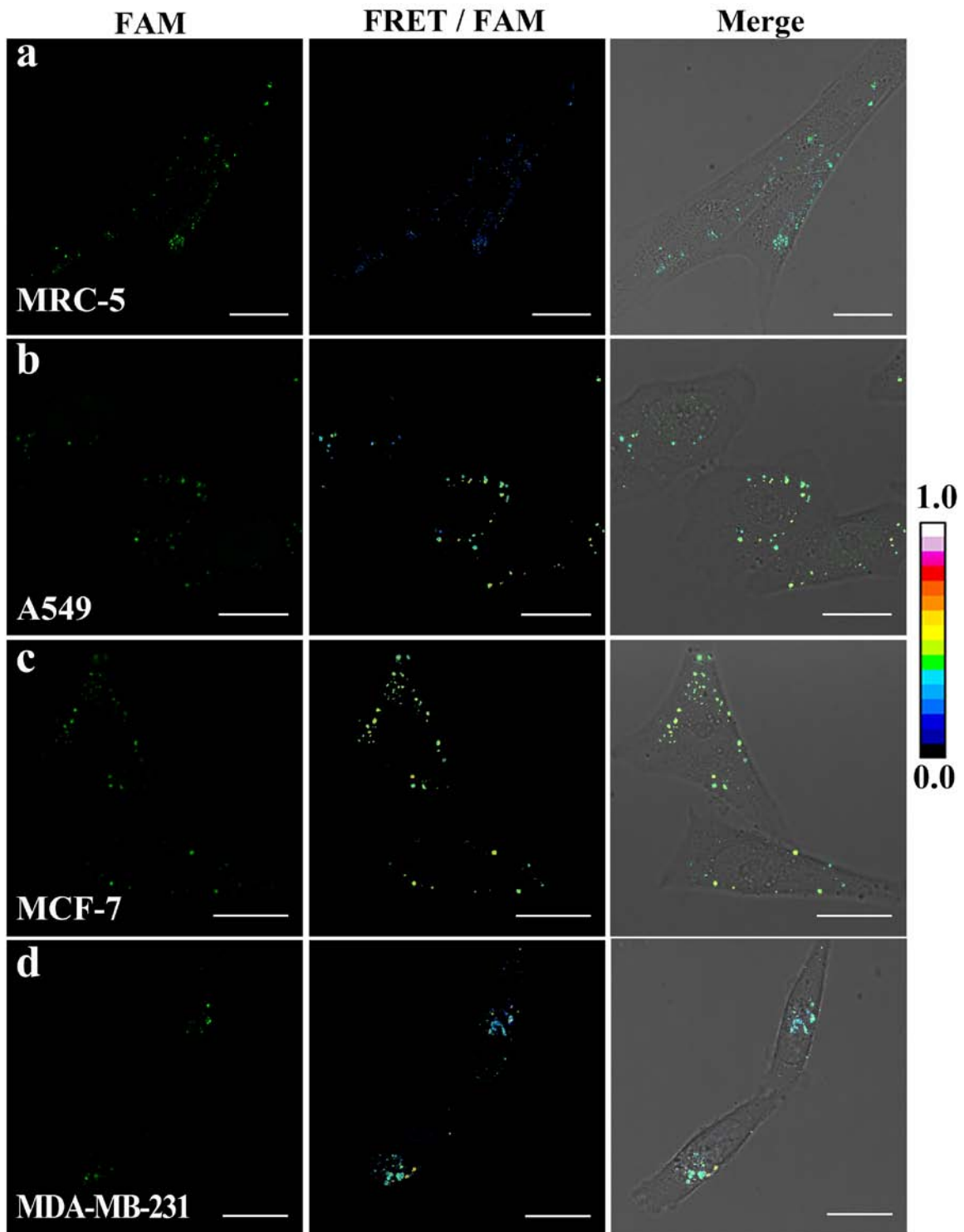
Figure S11. Living cell analysis of miRNAs-initiated OR logic gate operating and FRET transduction. Cells were transfected with the OR gate then imaged after 3h.
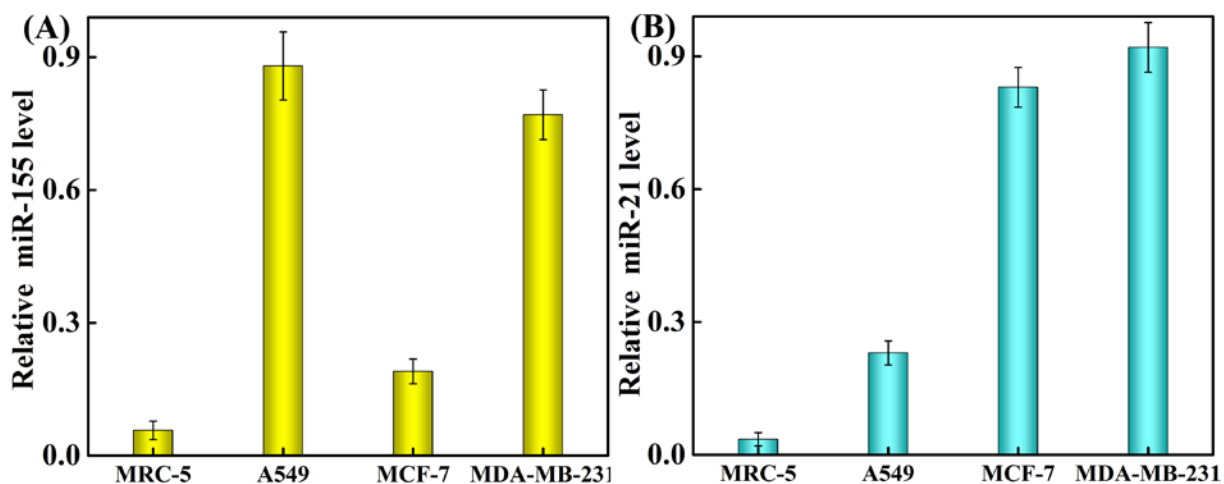
Figure S12. Relative expression levels of miR-155 (A) and miR-21 (B) in MRC-5, A549, MCF-7 and MDA-MB-231 cells.

Meanwhile, the different miRNAs (miR-21 and miR-155) expression levels of MRC-5, A549, MCF-7 and MDA-MB-231 cells were then determined by qRT-PCR (Figure S12). The qRT-PCR analysis of the above four cell lines indicated that A549 and MCF-7 cells show a relatively high expression level of endogenous miR-155 and miR-21, respectively, while MDA-MB-231 shows simultaneously overexpressed miR-155 and miR-21, which is consistent with the intracellular imaging result. Therefore, the designed cascaded HCR biocomputing system can sense the fluctuated expression and distribution of tumor-related miRNAs in different living cells and can be used to distinguish different cell lines, implying the potential applications in accurate diagnosis and programmable therapeutics.
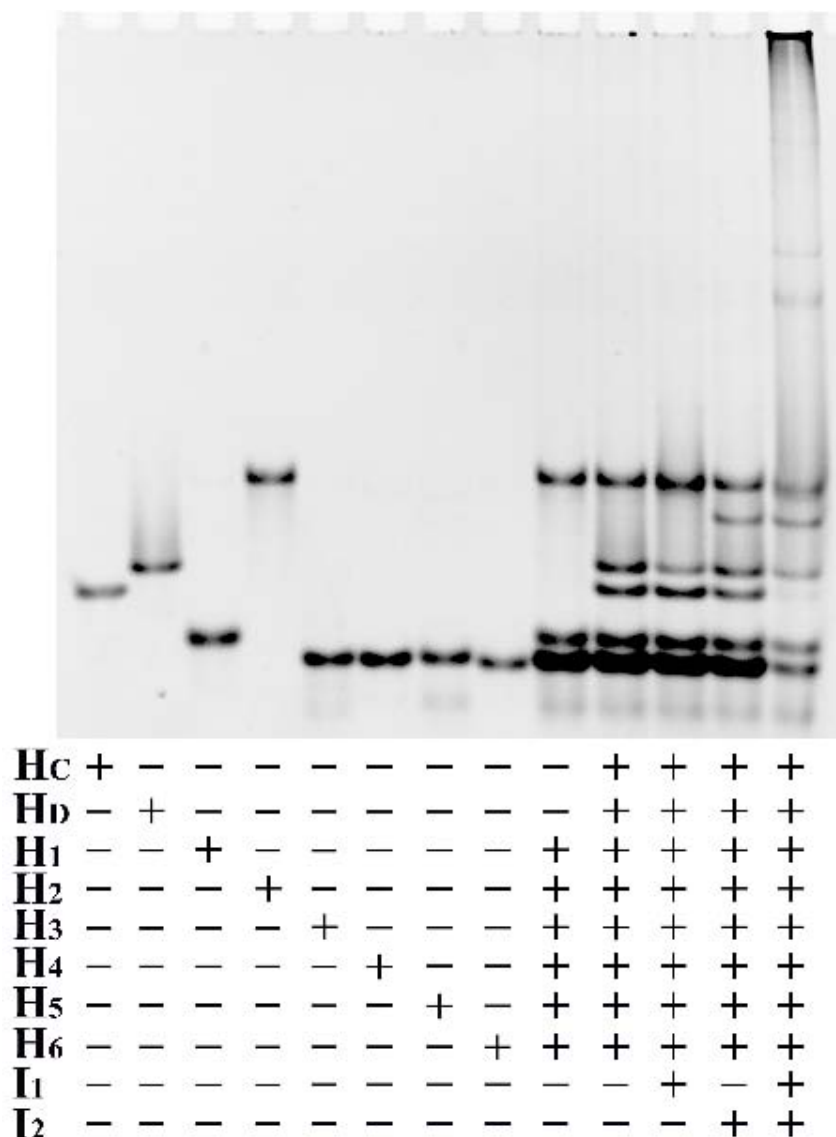
MiRNAs-initiated AND gate

Hc	+	−	−	−	−	−	−	−	−	+	+	+	+
HD	−	+	−	−	−	−	−	−	−	+	+	+	+
H1	−	−	+	−	−	−	−	−	+	+	+	+	+
H2	−	−	−	+	−	−	−	−	+	+	+	+	+
H3	−	−	−	−	+	−	−	−	+	+	+	+	+
H4	−	−	−	−	−	+	−	−	+	+	+	+	+
H5	−	−	−	−	−	−	+	−	+	+	+	+	+
H6	−	−	−	−	−	−	−	+	+	+	+	+	+
I1	−	−	−	−	−	−	−	−	−	−	+	−	+
I2	−	−	−	−	−	−	−	−	−	−	−	+	+

Figure S13. Native gel electrophoresis characterization of the AND logic gate. The "+" and "-" denote the presence and absence of the corresponding nucleic acid components, respectively.

Native PAGE analysis demonstrate that only the presence of both input, I_1 and I_2, the bands corresponding to the hairpin DNAs become weak and a band close to the notch with much higher molecular weight is generated (Figure S13), indicating the formation of more complex DNA nanostructure. The fluorescence and PAGE results are consistent with the truth table of AND gate, indicating the feasibility of the designed miRNA-initiated AND gate.
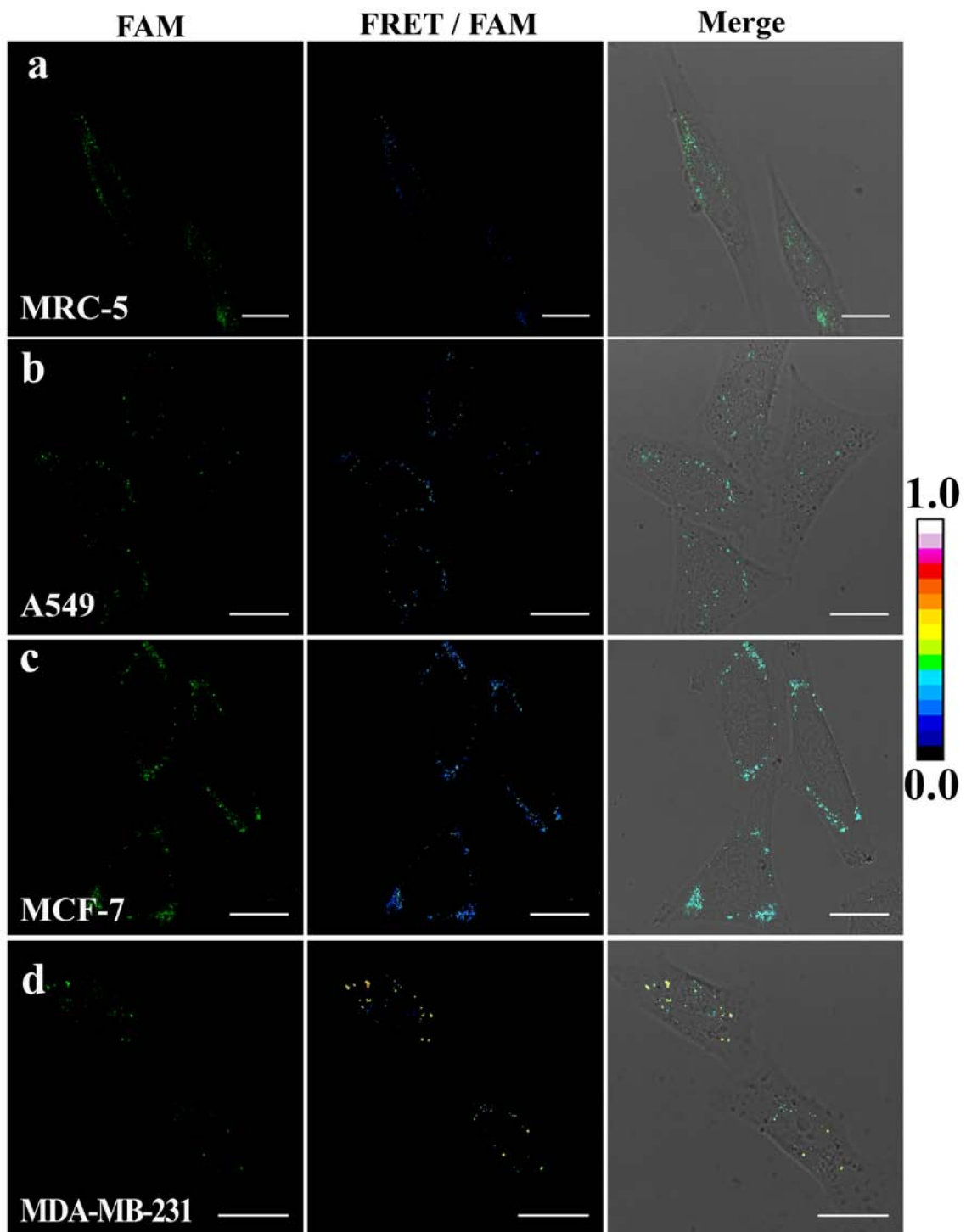
Figure S14. Living cell analysis of miRNAs-initiated AND logic gate operating and FRET transduction. Cells were transfected with the AND gate then imaged after 3h.
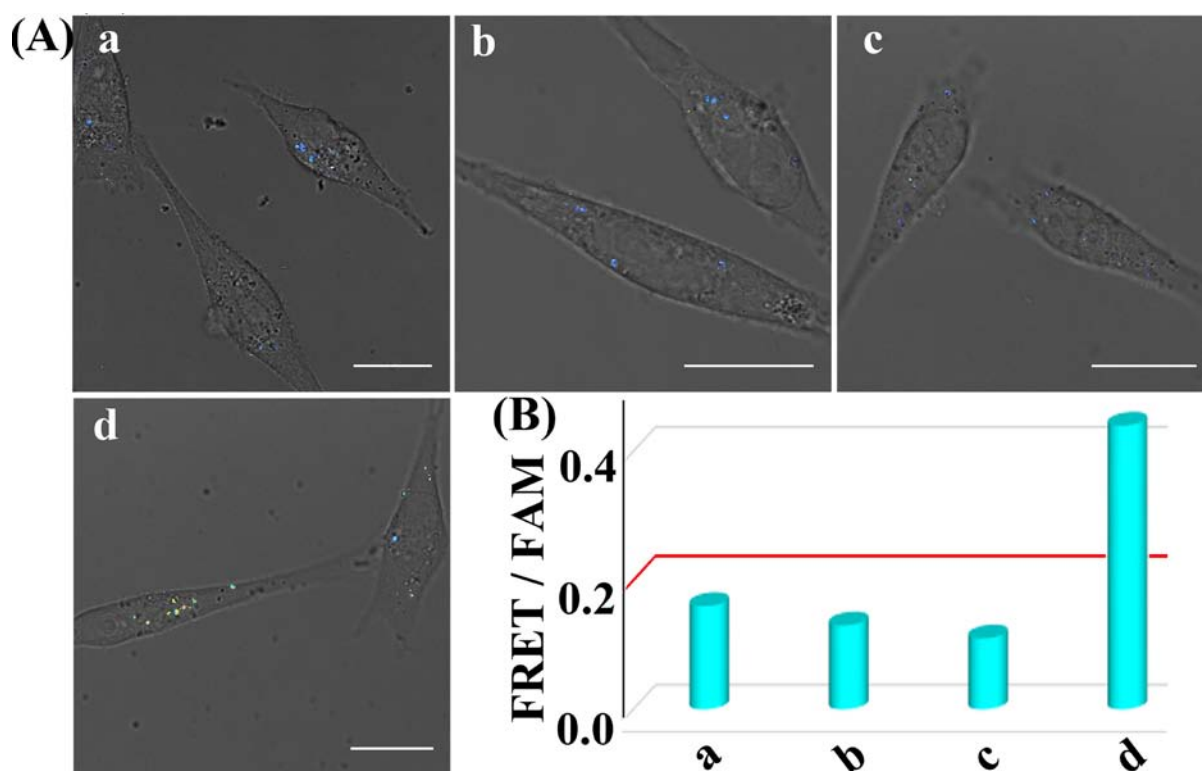
Figure S15. (A) CLSM imaging (in the form of FRET/FAM) of MDA-MB-231 cells treated with chemically modified (a) miR-155 inhibitor, (b) miR-21 inhibitor, (c) miR-155 and miR-21 inhibitor. (d) Routine MDA-MB-231 cells treated with AND logic gate DNA components. All scale bars correspond to 20 μm. **(B)** Statistical histogram analysis of the relative fluorescence intensity (FRET/FAM) of the above four cell samples.

For cancerous diagnose purpose, our AND logic gate was execrated in MDA-MB-231 cells. An apparent FRET signal was observed after transfected the sensing and processing modules (sample d of Figures S15 and S16), indicating the present system is activated through endogenous miRNAs. However, insignificantly FRET signal were obtained when the miR-155/21 expression were knocked down by introducing anti-miRNA inhibitor oligonucleotide into MDA-MB-231 cells (samples a, b and c of Figures S15 and S16), confirming the FRET signals are specifically induced by endogenous miR-155 (I_1) and miR-21(I_2). The results here clearly demonstrate that our designed miRNAs-initiated AND logic gate can generally operate in complex cellular environment, suggesting the great potential for early clinic diagnosis.
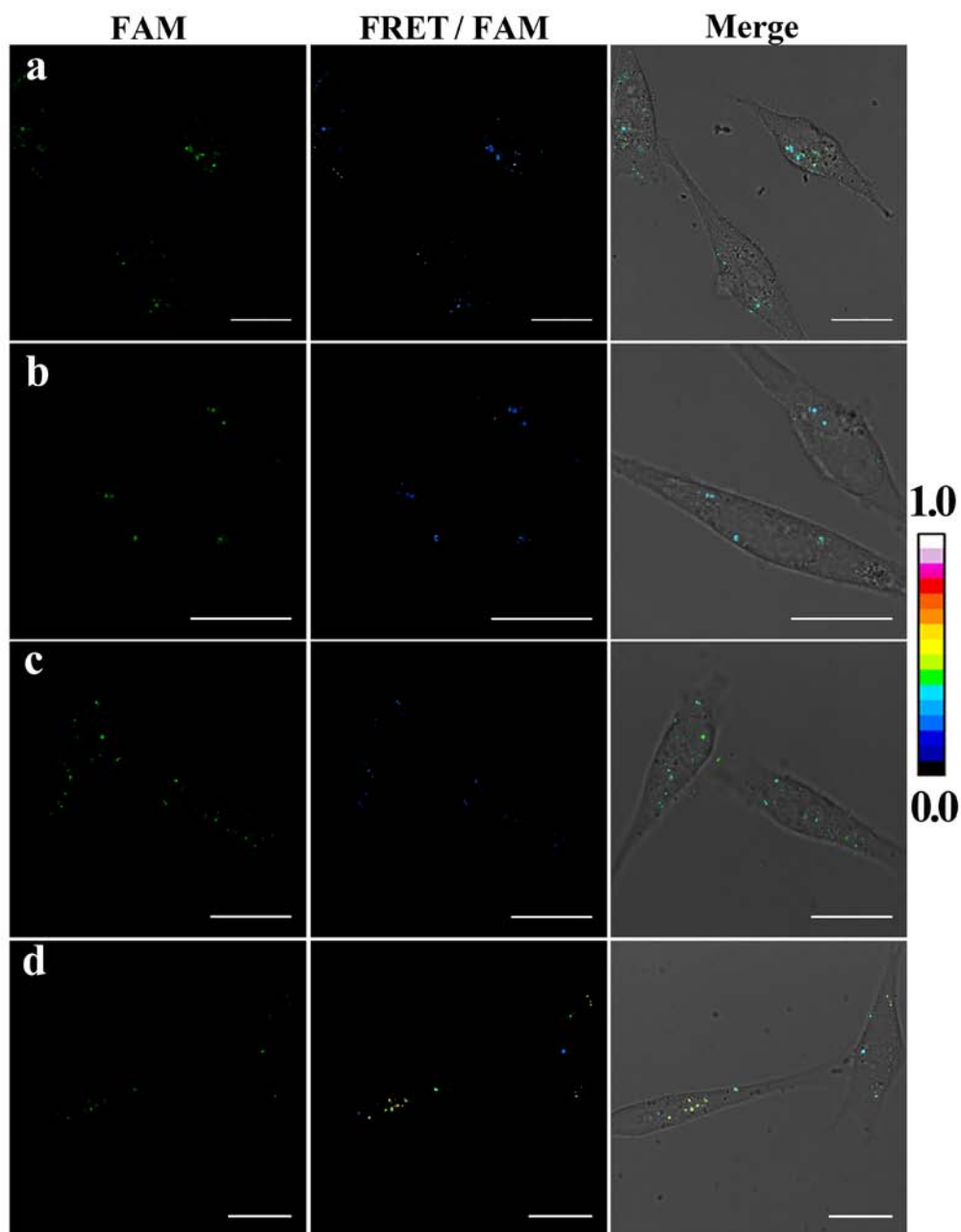
Figure S16. CLSM imaging (in the form of FRET/FAM) of MDA-MB-231 cells treated with chemically modified (a) miR-155 inhibitor, (b) miR-21 inhibitor, (c) miR-155 and miR-21 inhibitor. (d) Routine MDA-MB-231 cells treated with AND logic gate DNA components. All scale bars correspond to 20 μm.
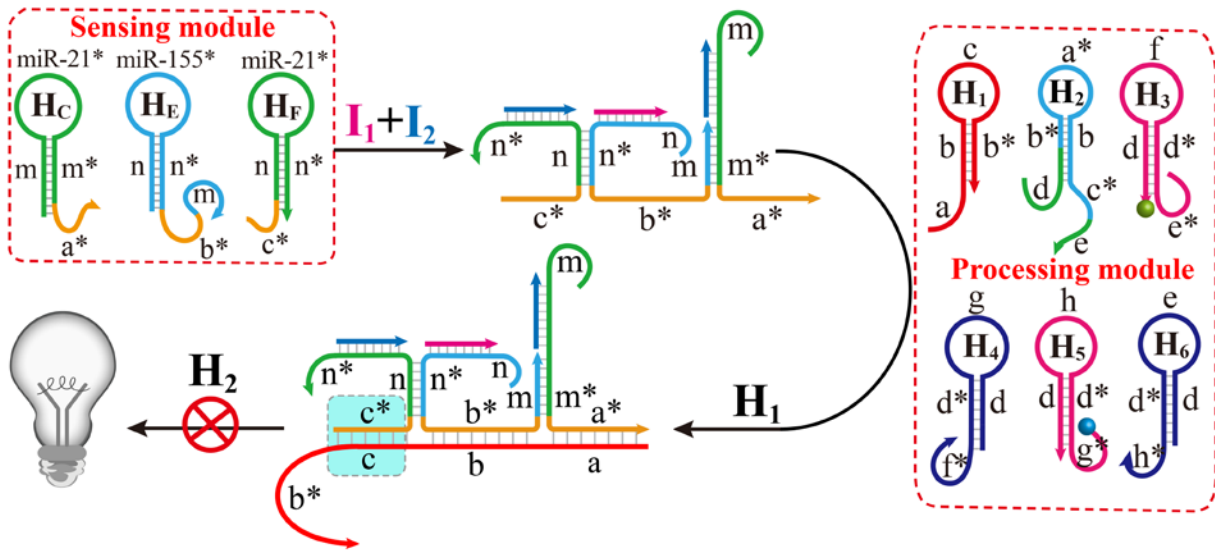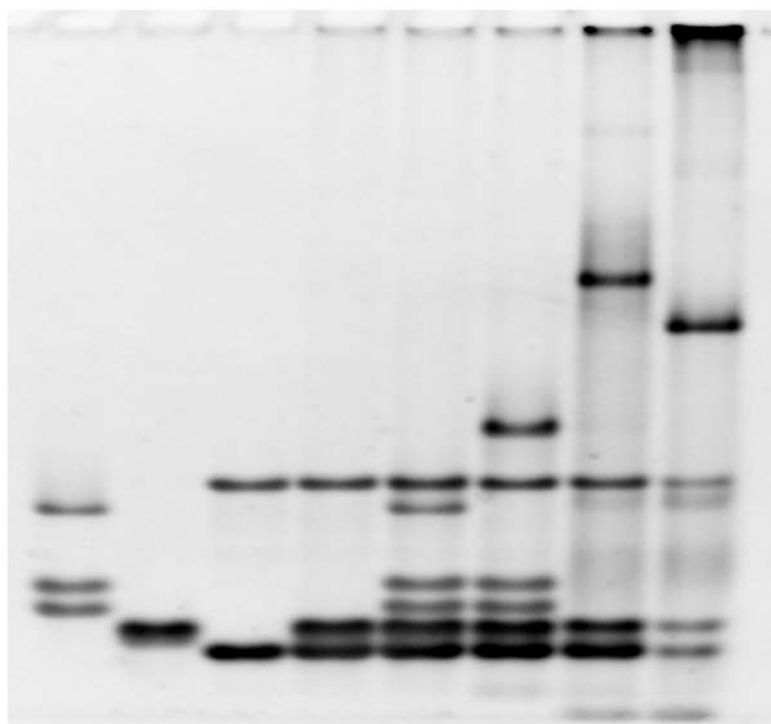
MiRNAs-initiated INHIBIT gate

Figure S17. The scheme of the INHIBIT logic gate in the presence of I_1 and I_2 inputs as shown in Figure 4A.

H_C	+	−	−	−	+	+	+	+
H_E	+	−	−	−	+	+	+	+
H_F	+	−	−	−	+	+	+	+
H_1	−	+	−	+	+	+	+	+
H_2	−	−	+	+	+	+	+	+
H_3	−	+	−	+	+	+	+	+
H_4	−	−	+	+	+	+	+	+
H_5	−	+	−	+	+	+	+	+
H_6	−	−	+	+	+	+	+	+
I_1	−	−	−	−	−	+	+	−
I_2	−	−	−	−	−	−	+	+

Figure S18. Native gel electrophoresis characterization of the INHIBIT logic gate. The "+" and "-" denote the presence and absence of the corresponding nucleic acid components, respectively.

The behavior of the designed INHIBIT logic gate was also analyzed by native PAGE. As presented in Figure S18, the formation of high molecular DNA nanostructure can be observed only the presence of I_2 input, which is consistent with a characteristic of INHIBIT gate.
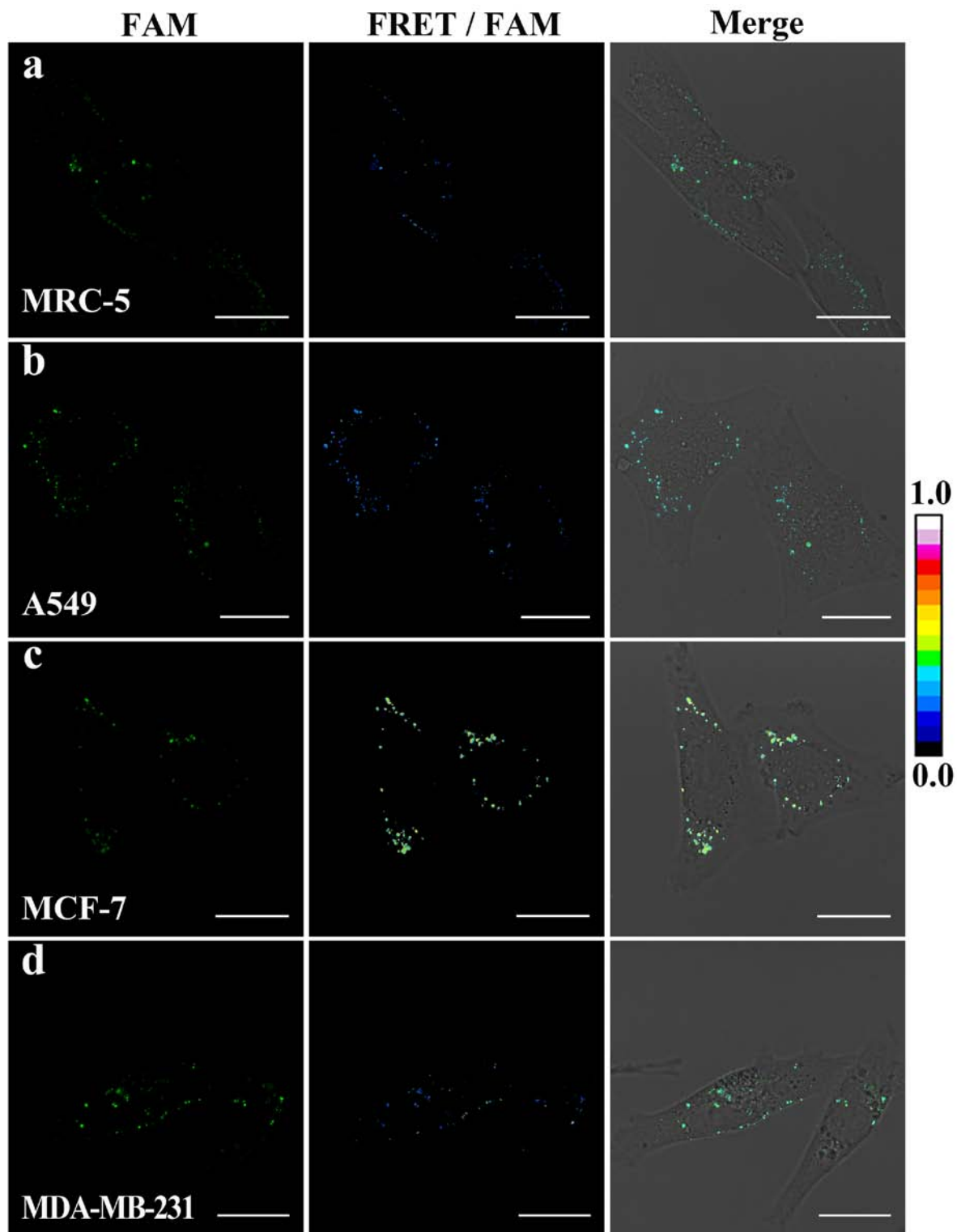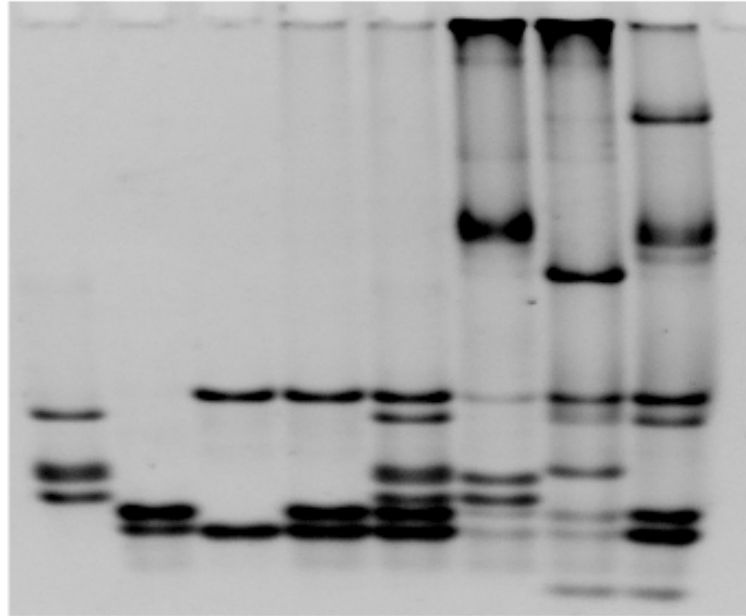
Figure S19. Living cell analysis of miRNAs-initiated INHIBIT gate operating and FRET transduction. Cells were transfected with the INHIBIT gate then imaged after 3h.

MiRNAs-initiated XOR gate operating

H_B +	−	−	−	+	+	+	+
H_C +	−	−	−	+	+	+	+
H_E +	−	−	−	+	+	+	+
H_F +	−	−	−	+	+	+	+
H_1 −	+	−	+	+	+	+	+
H_2 −	−	+	+	+	+	+	+
H_3 −	+	−	+	+	+	+	+
H_4 −	−	+	+	+	+	+	+
H_5 −	+	−	+	+	+	+	+
H_6 −	−	+	+	+	+	+	+
I_1 −	−	−	−	−	+	−	+
I_2 −	−	−	−	−	−	+	+

Figure S20. Native gel electrophoresis characterization of the XOR gate system. The "+" and "-" denote the presence and absence of the corresponding nucleic acid components, respectively.

Native PAGE verification of the XOR gate further demonstrated that the Truth output is generated only upon activation by miR-155 (I_1) or miR-21 (I_2) alone (Figure S20), which is consistent with the fluorescence assay of Figure 4B.
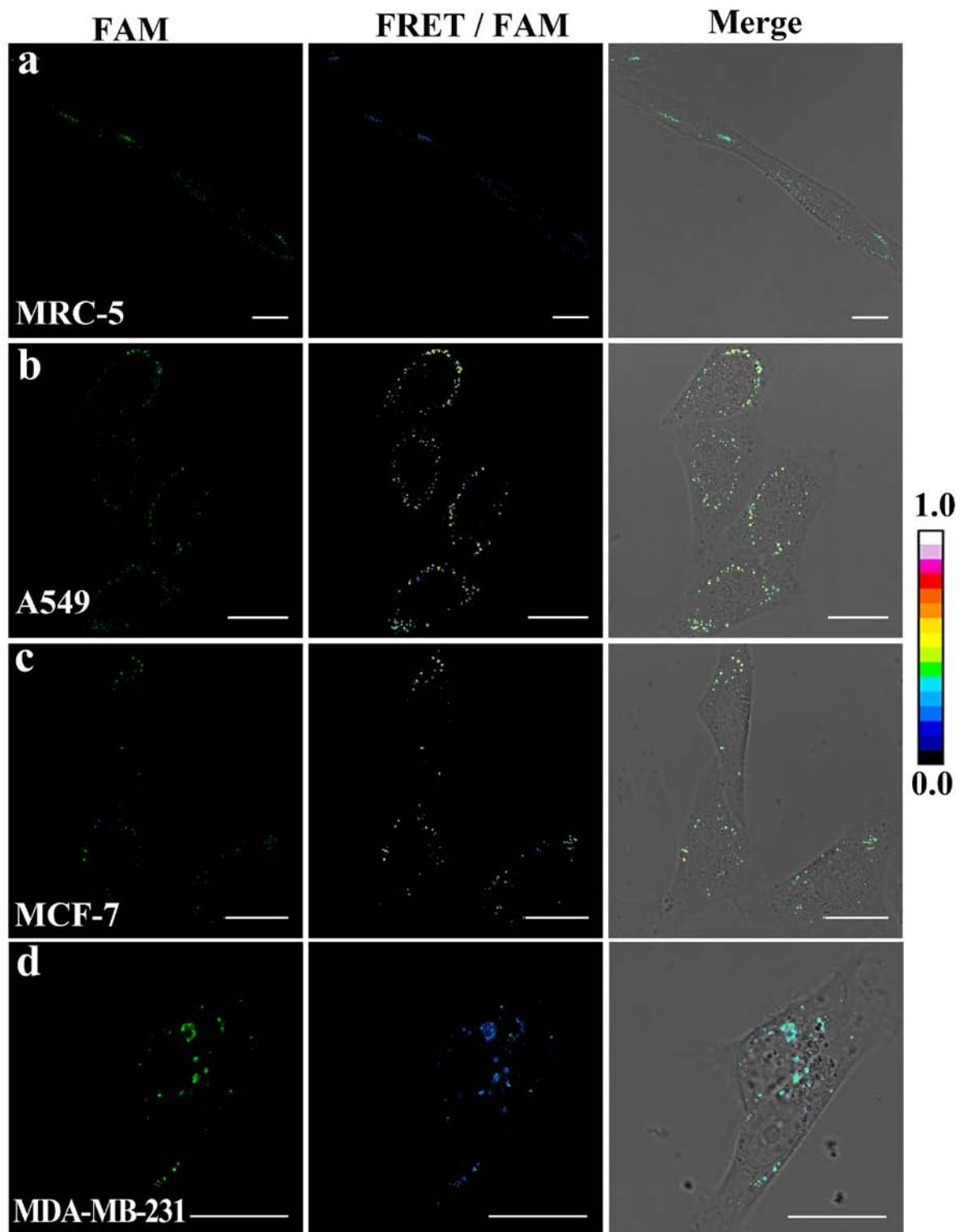
Figure S21. Living cell analysis of miRNAs-initiated XOR gate operating and FRET transduction. Cells were transfected with the XOR gate then imaged after 3h.

FRET efficiency of the XOR-imaging system

To evaluation the reliable FRET efficiency of the miRNAs-powered XOR gate, acceptor-photo-bleaching technique was performed. In a typical Föster Resonance Energy Transfer (FRET) process, an excited fluorophore (donor) transfers its excited state energy to a light-absorbing molecule (acceptor) in a non-radiative way. In the presented system, the FAM (donor) fluorescence could be recovered after photobleaching of the TAMRA (acceptor). The difference in the intensity of the donor before and after acceptor-photobleaching gives a direct indication of the FRET efficiency ($FRET_{eff}$) and can be quantified as follows:

$FRET_{eff} = (D_{post} - D_{pre})/D_{post}$

where D_{pre} and D_{post} correspond to thefluorescence intensities of FAM donor before and after TAMRA-photobleaching, respectively.

The mean FRET efficiency is obtained with the protocol provide by Leica wizards Application Suite Advanced Fluorescence (LAS AF). In brief, a 488 nm laser is used as the excitation source of the green channel of fluorophore (FAM) donor with an accompanying emission ranging from 500 to 550 nm. An external 561 nm excitation is chosen for the red channel of TAMRA (acceptor) fluorophore with an accompanying emission ranging from 570 to 640 nm. Then, we draw a region of interest (ROI) around these cells and select the number of bleaching iteration as 10. The FRET efficiency within the bleached region (ROI) is obtained after running the bleaching operation. The mean FRET efficiency of A549 and MCF-7 are determined by photobleaching randomly selected living cells of large quantities.

As displayed in Figure S22 and Figure S23, the red acceptor signal (TAMRA) tends to decrease while the green donor signal (FAM) becomes more obvious after photobleaching, which is due to an effective FRET from FAM to TAMRA originated from the miRNA-initiated biocomputing system in living cells. The average FRET efficiency are calculated to be 0.54 and 0.57 for A549 and MCF-7 cancer cells, respectively.
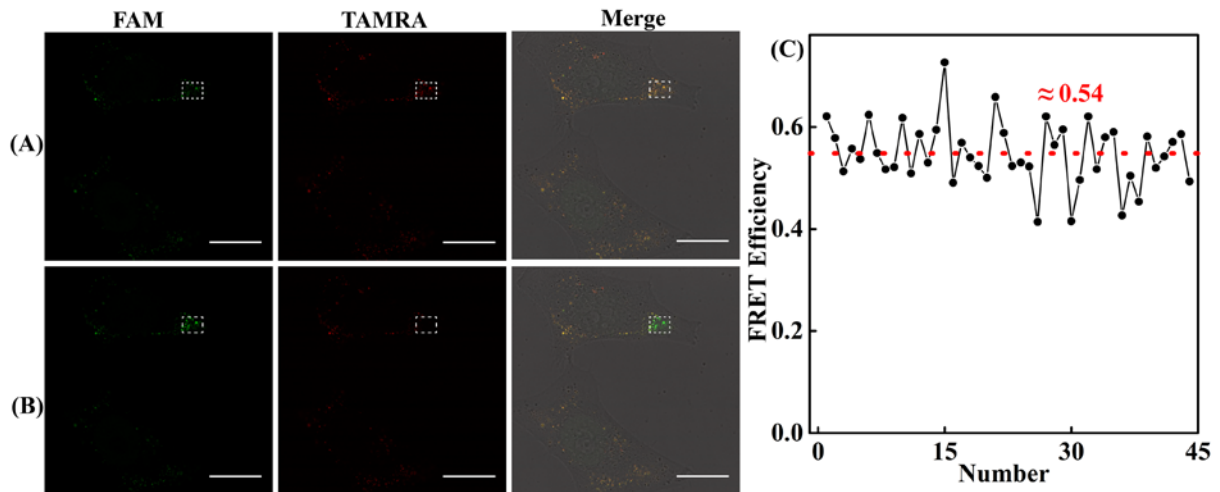
Figure S22. Evaluation of the FRET efficiency of the miR-155-initiated XOR gate system. CLSM imaging of miR-155-initiated XOR gate in A549 living cells before **(A)** and after **(B)** photobleaching of TAMRA acceptor. **(C)** The average FRET efficiency of the system collected from a large number of A549 living cells.
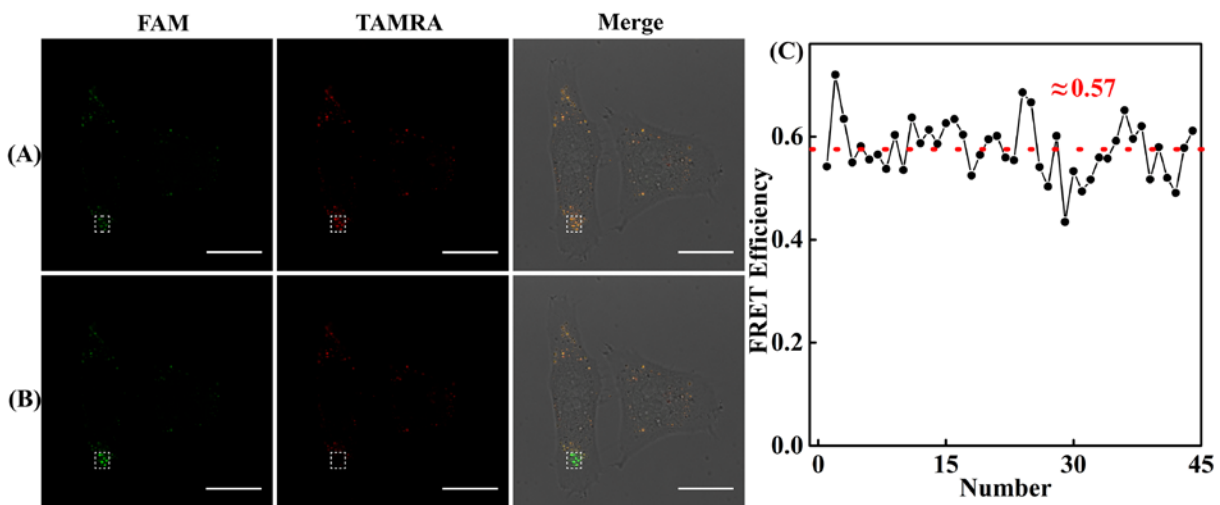

Figure S23. Evaluation of the FRET efficiency of the miR-21-initiated XOR gate system. CLSM imaging of miR-21-initiated XOR gate in MCF-7 living cells before **(A)** and after **(B)** photobleaching of TAMRA acceptor. **(C)** The average FRET efficiency of the system collected from a large number of MCF-7 living cells.
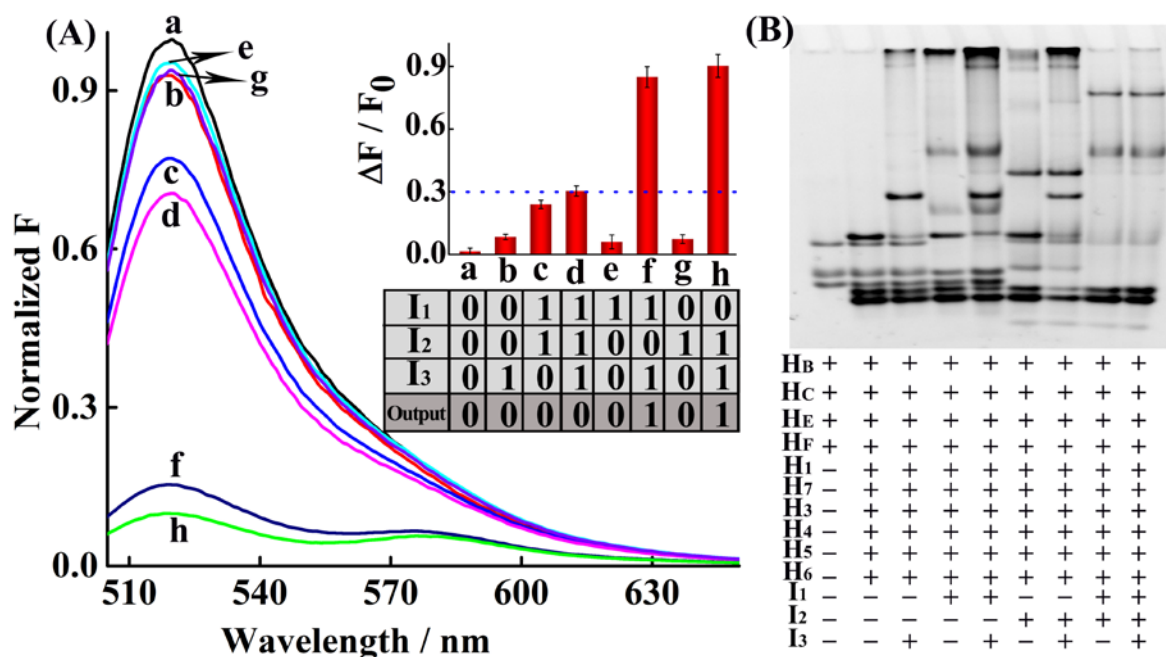
XOR-AND biocircuit

Figure S24. (A) Normalized fluorescence spectra of the XOR-AND biocircuit. Inset: the bar presentation and Truth table of the biocomputing system. F_0 is the fluorescence of the non-triggered system and F corresponds to the input-triggered system. **(B)** Native gel electrophoresis characterization of the XOR-AND biocircuit. The "+" and "-" denote the presence and absence of the corresponding nucleic acid components, respectively.

According to the results in Figure S24A, only the presence of input I_1 or I_2 and I_3 can activate the designed biocomputing circuit and exhibit significantly decrease in fluorescence intensity, while the addition of other input shows negligible changes in fluorescence intensity compared to the blank test, indicating the successful implementation of the engineered XOR-AND biocomputing circuit. To better confirm the XOR-AND biocircuit operation, native PAGE was implemented according to Figure S24B. When either I_1 or I_2 input was introduced, a new band with lower electrophoretic mobility were emerged for upstream HCR-1. Addition of I_3 input result in the generation of a bright bands with a maximum size of tens of thousands of base-pairs, suggesting the production of high-molecular-weight dsDNA products. These results herein clearly demonstrate that our designed XOR-AND circuit may be suitable for amplified detection of low abundant multiplex analyte.
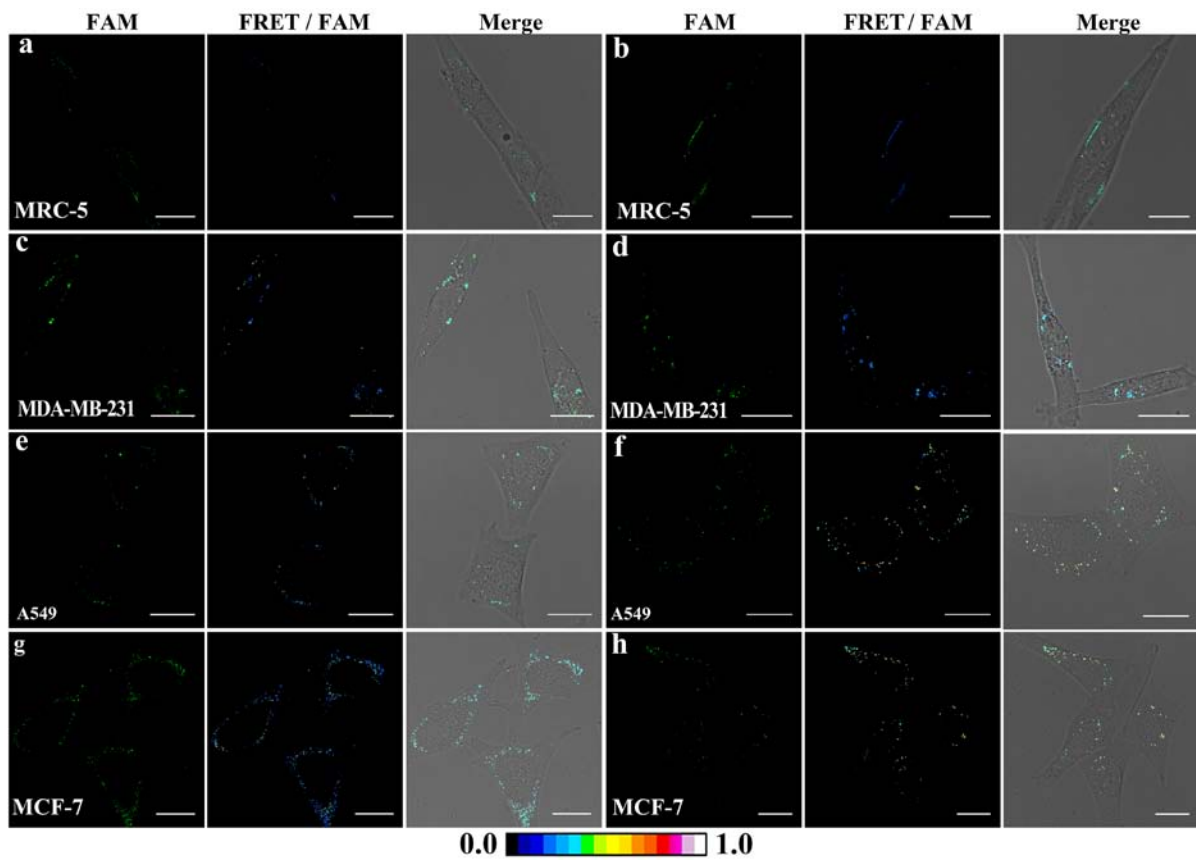
Figure S25. Living cell analysis of miRNAs-initiated XOR-AND biocircuit operating and FRET transduction in (a) intact MRC-5, (b) **I₃** pretreated MRC-5, (c) intact MDA-MB-231, (d) **I₃** pretreated MDA-MB-231, (e) intact A549, (f) **I₃** pretreated A549, (g) intact MCF-7, (h) **I₃** pretreated MCF-7.

XOR-INHIBIT biocircuit

An integrated XOR-INHIBIT biocircuit was developed according to Figure S26A. The input I_4 can hybridize with the tandem trigger T, resulting in False output due to the prohibiting the efficient generation of FRET signal. The dependence of fluorescence intensity upon the presence of different input was investigated. According to Figure S26B, the presence of I_4 input leads to False output. Meanwhile, PAGE analysis was also implemented to validate the effects of the XOR-INHIBIT biocircuit (Figure S26C). In the absence of I_4 input, a bright band with much lower mobility on the notch is obtained, suggesting the system proceeded as designed upon encountering the proper input. Experimental verification the reliability of circuit function is highly in agreement with the truth table of literature report, indicating the great potential of the designed DNA biocircuit platform in clinical miRNA diagnostics.
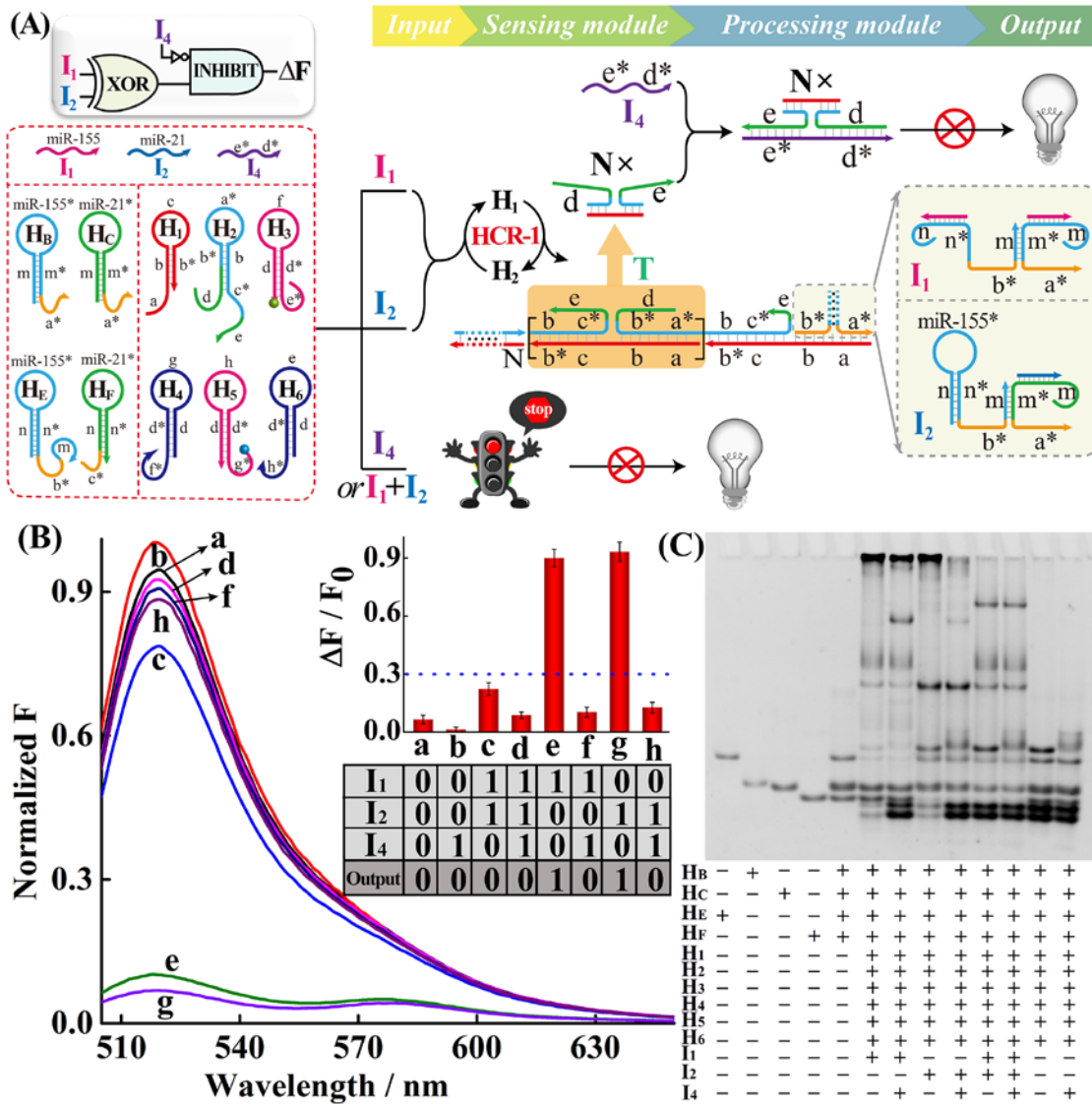
Figure S26. (A) Schematic representation of the XOR-INHIBIT biocomputing circuit device. **(B)** Normalized fluorescence spectra generated by the XOR-INHIBIT circuit. Insert: the bar presentation and Truth table of the XOR-INHIBIT circuit system. F_0 is the fluorescence of the system without any input, and F corresponds to the resulting fluorescence of the system after adding the respective inputs. **(C)** Native gel electrophoresis characterization of the XOR-INHIBIT gate system. The "+" and "-" denote the presence and absence of the corresponding miRNA or DNA components, respectively.
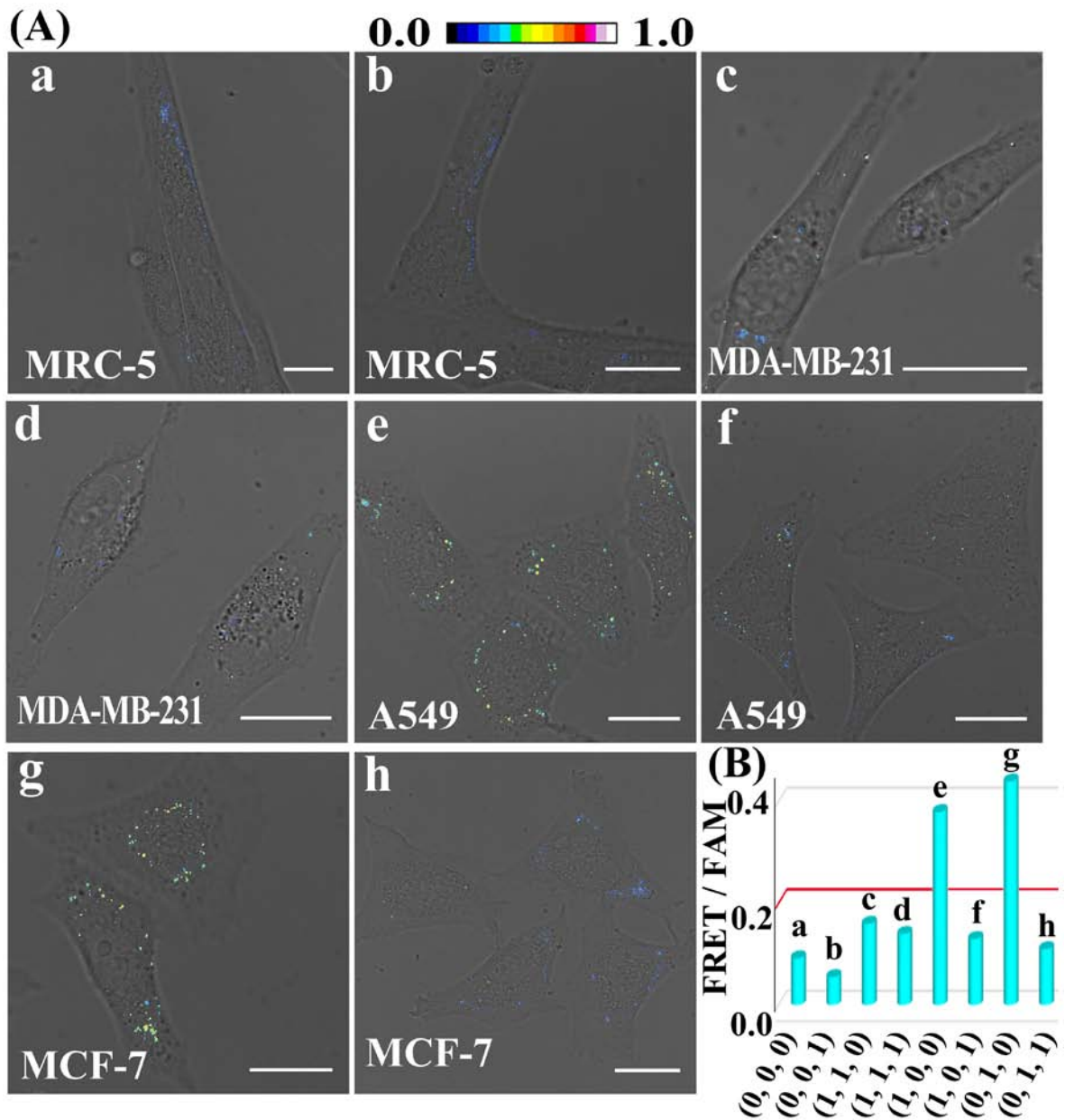
Figure S27. **(A)** Living cell analysis of different cell lines using the designed XOR-INHIBIT biocircuit to trace intracellular miRNAs activity in (a) intact MRC-5, (b) I_4 pretreated MRC-5, (c) intact MDA-MB-231, (d) I_4 pretreated MDA-MB-231, (e) intact A549, (f) I_4 pretreated A549, (g) intact MCF-7, (h) I_4 pretreated MCF-7. All scale bars correspond to 20 μm. **(B)** Statistical histogram analysis of the relative fluorescence intensity (FRET/FAM) of the above four cell lines through miRNAs-initiated XOR-INHIBIT biocircuit.
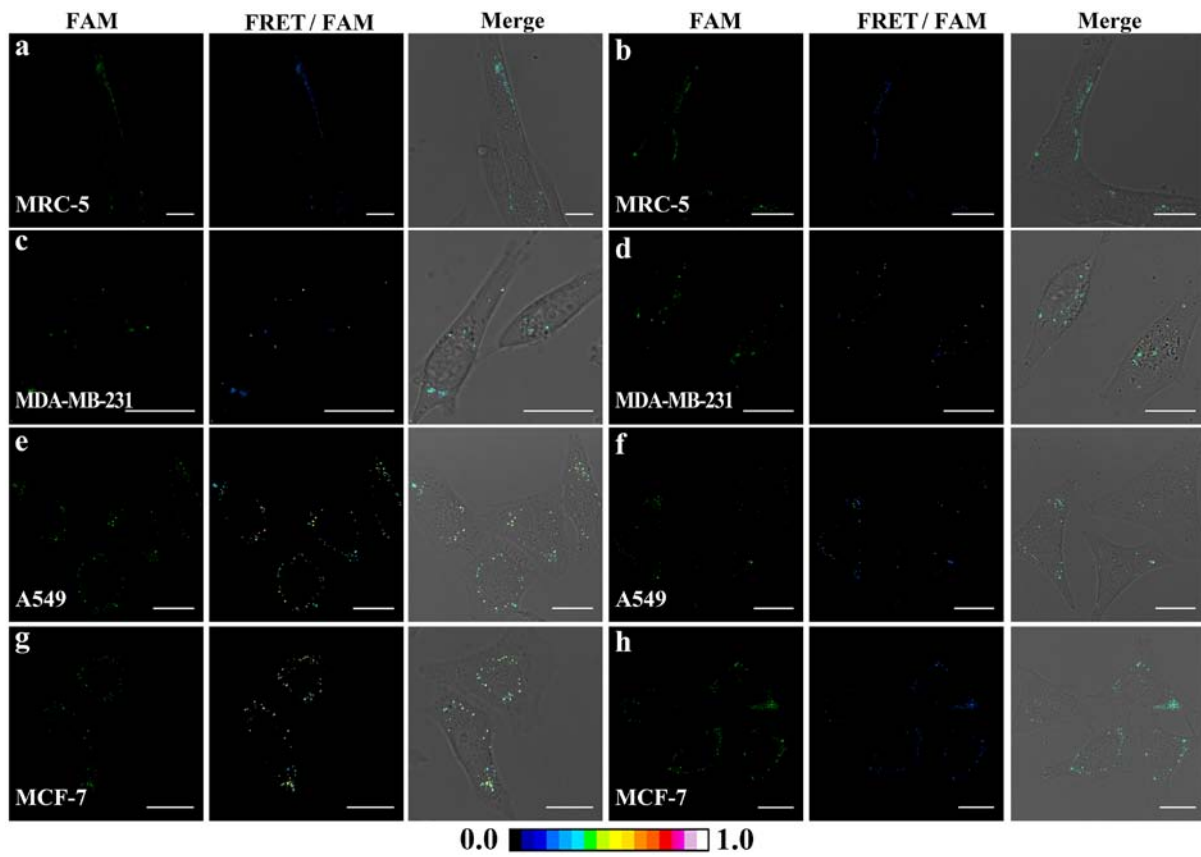
Figure S28. Living cell analysis of miRNAs-initiated XOR-INHIBIT biocircuit by FRET transduction in (a) intact MRC-5, (b) I_4 pretreated MRC-5, (c) intact MDA-MB-231, (d) I_4 pretreated MDA-MB-231, (e) intact A549, (f) I_4 pretreated A549, (g) intact MCF-7, (h) I_4 pretreated MCF-7.

MiRNAs-initiated XOR-OR biocircuit

To further demonstrate the information communication for the higher-order circuits with varying degrees of complexity, a XOR-OR biocomputing circuit is successfully realized according to Figure S29A. Pretreated the biosystem with input I_5, which was composed of domains **f** and **d**, the downstream HCR-2 can be motivated due to domain **f** was complementary with segment **f*** of H_4. Hence the downstream HCR-2 further triggers autonomous and repeated sequential cross-hybridization of H_3, H_4, H_5 and H_6 into dsDNA copolymers, which result in the donor (FAM) and acceptor (TAMRA) fluorophore pairs into close proximity and generates the fluorescence readout signal (Truth output).

According to the results shown in Figure S29B, upon introduction of input I_5 to the XOR-OR circuit resulted in a significantly decrease of FAM fluorescence intensity, whereas the absence of both three input leads to False output, suggesting accurate operation of the designed XOR-OR circuit in vitro. Figure S29C further exhibits the electrophoretic mobility in the presence of different inputs. These results highly demonstrate the reliability of the designed XOR-OR circuit.
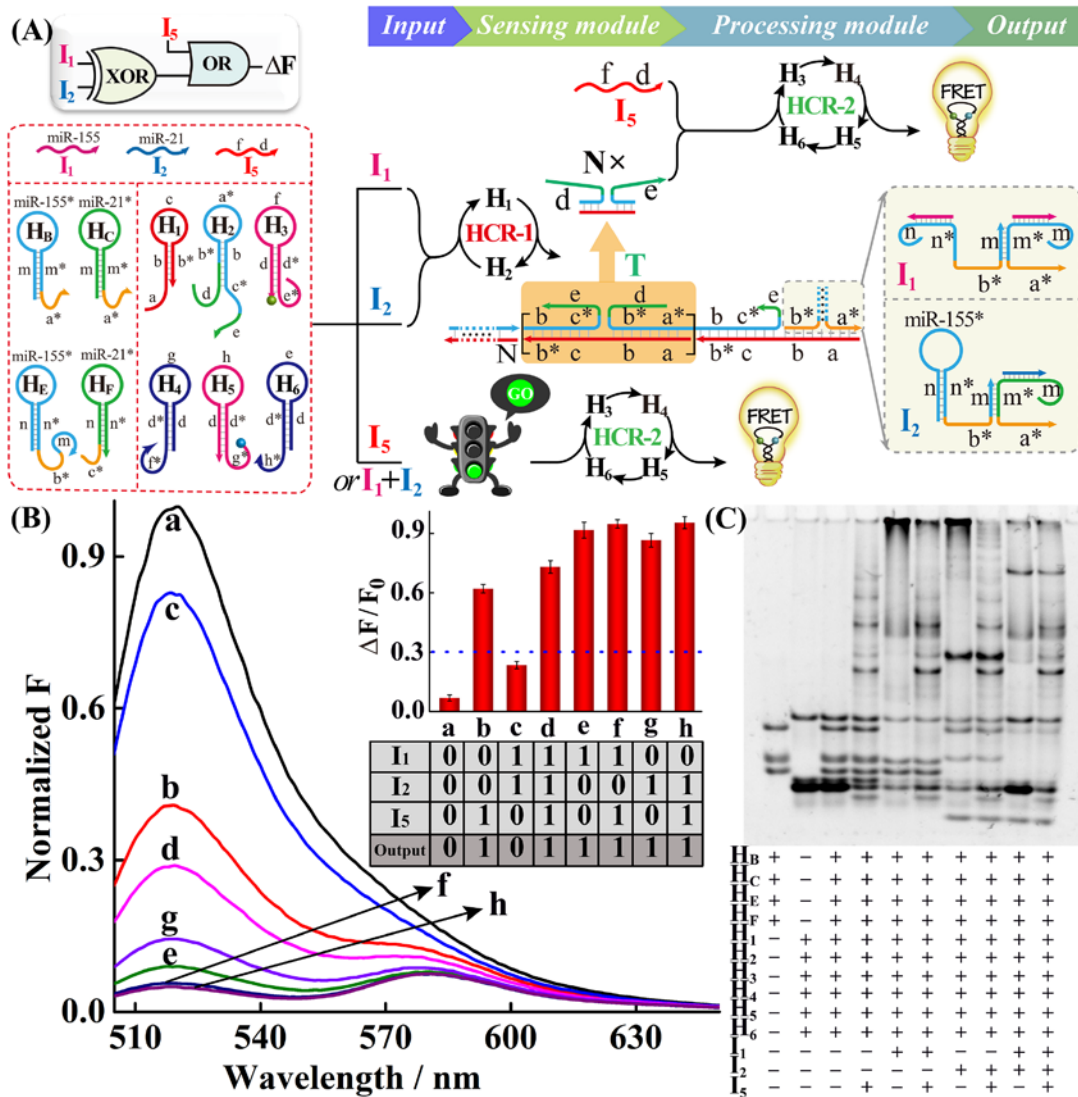
Figure S29. (**A**) Schematic representation of the XOR-OR biocomputing circuit device. (**B**) Normalized fluorescence spectra generated by the XOR-OR circuit system. Insert: the bar presentation and Truth table of the XOR-OR circuit system. F_0 is the fluorescence of the system without any input, and F corresponds to the resulting fluorescence of the system after adding the respective inputs. (**C**) Native gel electrophoresis characterization of the XOR-OR biocircuit system. The "+" and "-" denote the presence and absence of the corresponding miRNA or DNA components, respectively.
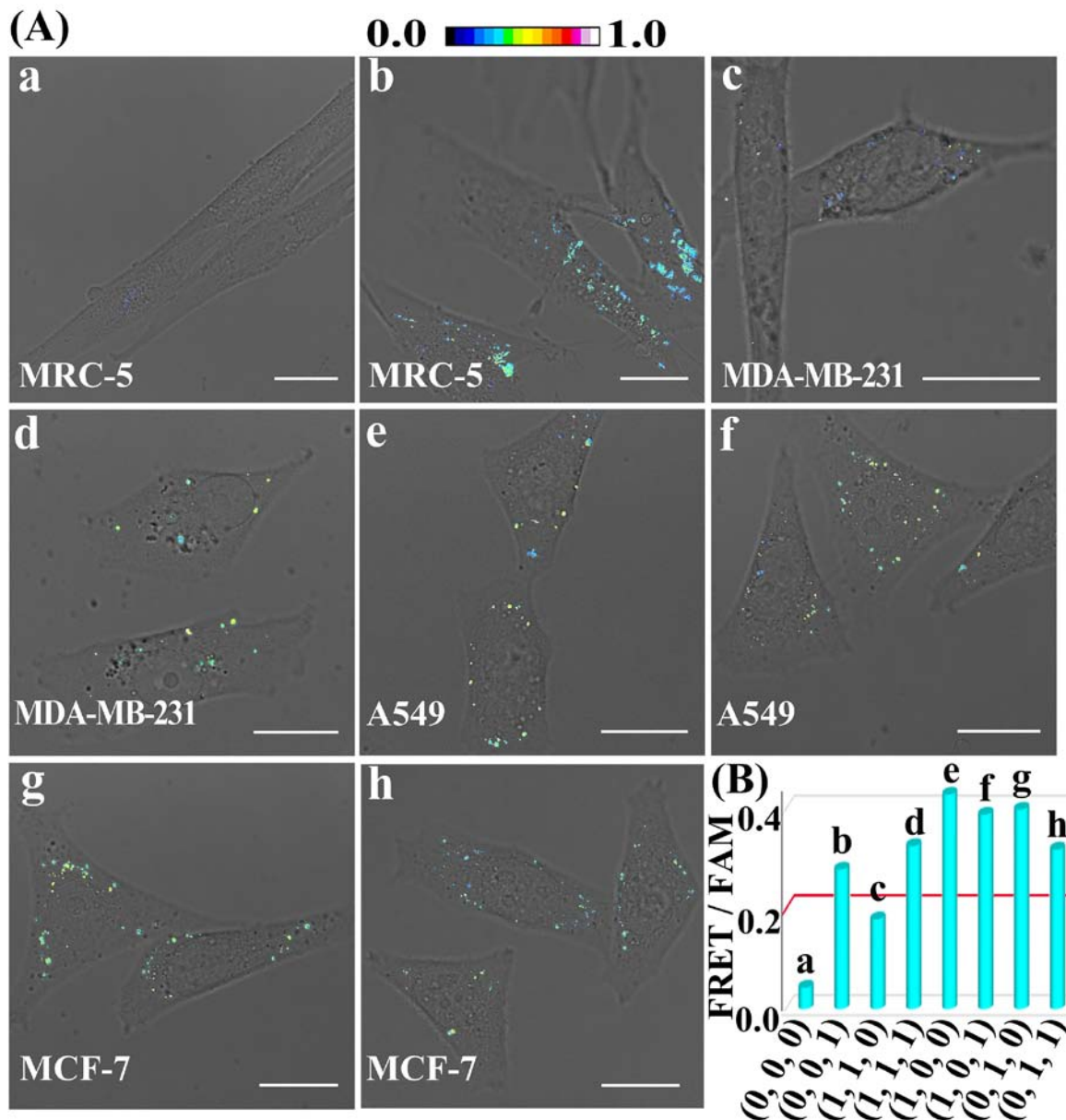
Figure S30. (A) Living cell analysis of different cell lines using the designed XOR-OR biocircuit to trace intracellular miRNA activity in (a) intact MRC-5, (b) I_5 pretreated MRC-5, (c) intact MDA-MB-231, (d) I_5 pretreated MDA-MB-231, (e) intact A549, (f) I_5 pretreated A549, (g) intact MCF-7, (h) I_5 pretreated MCF-7. All scale bars correspond to 20 μm. **(B)** Statistical histogram analysis of the relative fluorescence intensity (FRET/FAM) of the above four cell lines through miRNAs-initiated XOR-OR biocircuit.
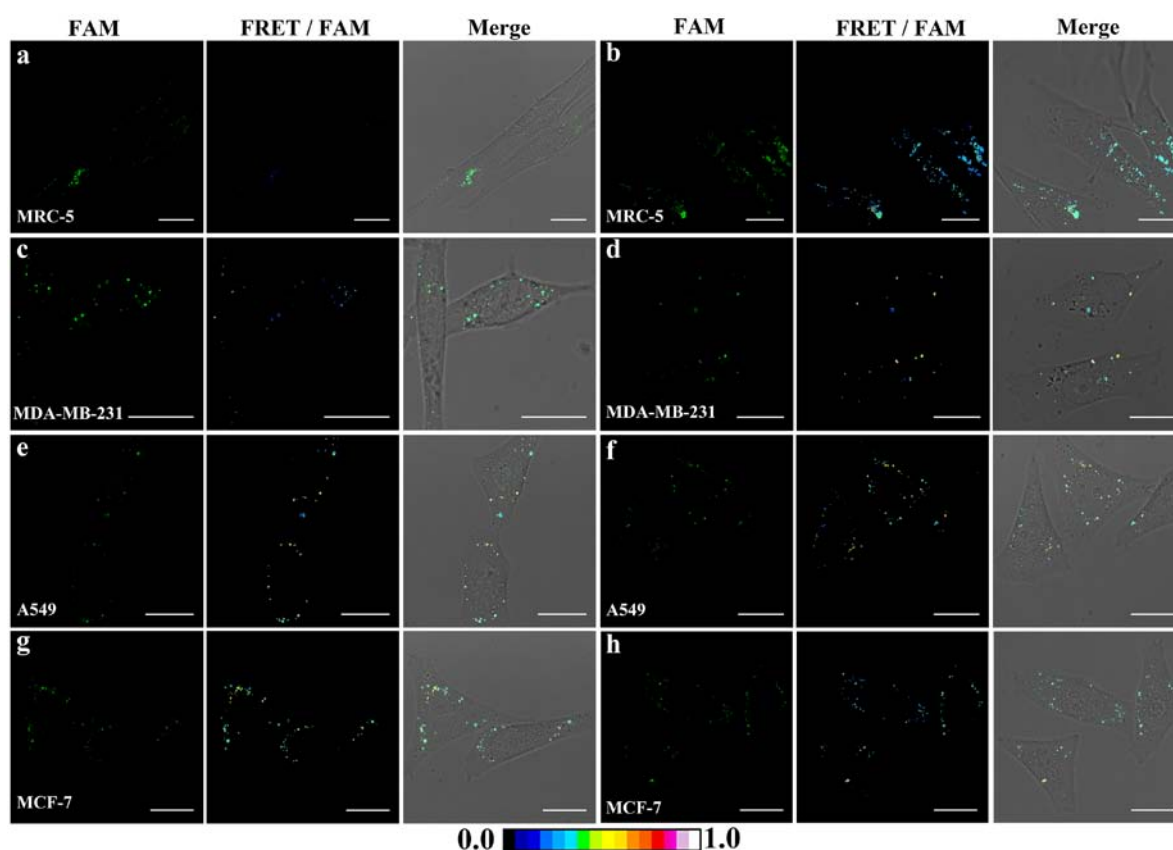
Figure S31. Living cell analysis of miRNAs-initiated XOR-OR biocircuit operating and FRET transduction in (a) intact MRC-5, (b) I_5 pretreated MRC-5, (c) intact MDA-MB-231, (d) I_5 pretreated MDA-MB-231, (e) intact A549, (f) I_5 pretreated A549, (g) intact MCF-7, (h) I_5 pretreated MCF-7.

Multiple-input genetic circuits could also be engineered in living cells by recognizing complex intracellular conditions, which is ideally suit for improve the sensing specificity and enhance sophisticated digital biological control. We experimentally tested the implementation of the XOR-OR circuit in four living cell types by transfected the DNA components and I_5 input. The output of each implemented function was analyzed by CLSM imaging (Figure S30 and S31). Endogenously express miRNA level was monitored by FRET transduction, which is highly agreement with the truth table of the XOR-OR circuit function, implying a potential application of the complicated biological information-processing devices.